Solid Earth Discuss., 6, 2523–2566, 2014
www.solid-earth-discuss.net/6/2523/2014/
doi:10.5194/sed-6-2523-2014
© Author(s) 2014. CC Attribution 3.0 License.

Solid Earth Discussions
Open Access

This discussion paper is/has been under review for the journal Solid Earth (SE).
Please refer to the corresponding final paper in SE if available.

Wave-equation based traveltime seismic tomography – Part 1: Method

P. Tong[1], D. Zhao[2], D. Yang[3], X. Yang[4], J. Chen[4], and Q. Liu[1]

[1]Department of Physics, University of Toronto, Toronto, M5S 1A7, Ontario, Canada
[2]Department of Geophysics, Tohoku University, Sendai, Japan
[3]Department of Mathematical Sciences, Tsinghua University, Beijing, China
[4]Department of Mathematics, University of California, Santa Barbara, California, USA

Received: 10 August 2014 – Accepted: 11 August 2014 – Published: 25 August 2014

Correspondence to: P. Tong (tongping85@gmail.com)

Published by Copernicus Publications on behalf of the European Geosciences Union.

Abstract

In this paper, we propose a wave-equation based traveltime seismic tomography method with a detailed description of its step-by-step process. First, a linear relationship between the traveltime residual $\Delta t = T^{\mathrm{obs}} - T^{\mathrm{syn}}$ and the relative velocity perturbation $\delta c(\boldsymbol{x})/c(\boldsymbol{x})$ connected by a finite-frequency traveltime sensitivity kernel $K(\boldsymbol{x})$ is theoretically derived using the adjoint method. To accurately calculate the traveltime residual Δt, two automatic arrival-time picking techniques including the envelop energy ratio method and the combined ray and cross-correlation method are then developed to compute the arrival times T^{syn} for synthetic seismograms. The arrival times T^{obs} of observed seismograms are usually determined by manual hand picking in real applications. Traveltime sensitivity kernel $K(\boldsymbol{x})$ is constructed by convolving a forward wavefield $u(t,\boldsymbol{x})$ with an adjoint wavefield $q(t,\boldsymbol{x})$. The calculations of synthetic seismograms and sensitivity kernels rely on forward modelling. To make it computationally feasible for tomographic problems involving a large number of seismic records, the forward problem is solved in the two-dimensional (2-D) vertical plane passing through the source and the receiver by a high-order central difference method. The final model is parameterized on 3-D regular grid (inversion) nodes with variable spacings, while model values on each 2-D forward modelling node are linearly interpolated by the values at its eight surrounding 3-D inversion grid nodes. Finally, the tomographic inverse problem is formulated as a regularized optimization problem, which can be iteratively solved by either the LSQR solver or a non-linear conjugate-gradient method. To provide some insights into future 3-D tomographic inversions, Fréchet kernels for different seismic phases are also demonstrated in this study.

1 Introduction

Seismic tomography is one of the core methodologies for imaging the structural heterogeneity of the Earth's interior at a variety of scales. Ever since the pioneering works of

SED
6, 2523–2566, 2014

Aki and Lee (1976) and Dziewonski et al. (1977), tomographic images have provided crucial information to the understanding of plate tectonics, volcanism and geodynamics (e.g. Romanowicz, 1991; Liu and Gu, 2012; Zhao, 2012). Seismic tomography itself also went through significant development over the last three decades, including advances in both methodology and data usage.

In the first two decades of its history, seismic tomography is mainly based on the ray theory which assumes that seismic traveltime is determined by the structure along the infinitely thin ray path only. However, because of scattering, wave front healing and other finite-frequency effects, seismic measurements (such as traveltime and amplitude), especially those made on broadband recordings, are sensitive to three-dimensional (3-D) structures off the ray path (e.g. Marquering et al., 1999; Dahlen et al., 2000; Tape et al., 2007). Ray theory is actually only valid when the scale length of the variation of material properties is much larger than the seismic wavelength (Rawlinson et al., 2010). To take into account the influence of off-ray structures, finite-frequency tomography methods in which 2-D or 3-D traveltime and amplitude sensitivity kernels are constructed, including those based on the paraxial approximation and dynamic ray tracing (e.g. Marquering et al., 1999; Dahlen et al., 2000; Tian et al., 2007; Tong et al., 2011) and those based on the normal mode theory (e.g. Zhao et al., 2000; Zhao and Jordan, 2006; To and Romanowicz, 2009). Tomographic models with improved resolutions were reported by recent finite-frequency tomographic studies (e.g. Montelli et al., 2004; Hung et al., 2004, 2011; Gautier et al., 2008), although comparison to ray-based tomography remains controversial (de Hoop and van der Hilst, 2005a; Dahlen and Nolet, 2005; de Hoop and van der Hilst, 2005b). The underlying problem of the finite-frequency tomography based on paraxial approximation and dynamic ray tracing is that its kernel computation still relies on the ray theory, although it was devised to account for non-geometrical finite-frequency phenomena. In the last decade or so, rapid advances in high-performance computing and forward modelling techniques make it feasible to solve the seismic wave equations in realistic Earth models by full numerical methods (e.g. Komatitsch and Tromp, 2002a, b; Komatitsch et al., 2004; Operto

SED
6, 2523–2566, 2014

et al., 2007). This opens the way to compute sensitivity kernels based on numerical simulation of the full seismic wavefield, avoiding the use of approximate theories (e.g. Liu and Tromp, 2006, 2008; Fichtner et al., 2009). It also made the conceptual wave-equation based seismic inversion methods such as the one presented by Tarantola (1984) feasible in realistic applications (Tape et al., 2009; Fichtner and Trampert, 2011; Zhu et al., 2012). To our best knowledge, adjoint tomography (Tromp et al., 2005; Fichtner et al., 2006), scattering integral methods (L. Zhao et al., 2005; Chen et al., 2007b), and full waveform inversion (FWI) in the frequency domain (Pratt and Shipp, 1999; Operto et al., 2006) are among the most popular tomographic techniques based upon solving full wave equations. FWI in frequency domain has been mainly used in exploration problems (e.g. Virieux and Operto, 2009; Lee et al., 2010) for relative small and regular simulation domains. Adjoint tomography and scattering integral tomography are closely related to each other, and a detailed comparison between adjoint tomography and scattering integral tomography can be found in Chen et al. (2007a). For brevity, we restrict our following discussions to adjoint tomography (Liu and Gu, 2012).

Adjoint tomography is currently one of the most popular and promising tomographic methods for resolving strongly varying structures. It takes advantages of full 3-D numerical simulations in forward modelling and sensitivity kernel calculation, often iteratively improves models through optimization techniques (Tromp et al., 2005; Tape et al., 2007). The use of full numerical simulations allows for the freedom of choosing either 1-D or 3-D reference models and accurate calculations of seismograms (Tong et al., 2014a) and sensitivity kernels for complex models (Liu and Tromp, 2006, 2008). Using this approach, Tape et al. (2009, 2010) obtained a 3-D velocity model of the southern California crust that captures strong local heterogeneity up to ±30 %. Similarly, Zhu et al. (2012) generated a tomographic model of the European upper mantle based on adjoint tomography that reveals nice correlations between structural features and regional tectonics and dynamics. Similarly, Rickers et al. (2013) presented a 3-D *S* wave velocity model of the North Atlantic region, revealing structural features in unprecedented detail down to the depth of 1300 km. These successful applications reveal

SED
6, 2523–2566, 2014

the promising future of next generation seismic tomographic models based on full numerical simulations. However, the expensive computation cost associated with adjoint-type of wave-equation-based tomographic methods, especially for 3-D problems, is still a major stumbling block to its wider applications. For example, for a moderate number of three-component seismograms, 0.8 million and 2.3 million central processing unit hours were used to generate the tomographic models of the southern California crust and the European upper mantle, respectively (Tape et al., 2009; Zhu et al., 2012). The severity of the cost issue may be remedied when simulations are ported to the Graphic Processing Unit (GPU) hardwares (e.g. Komatitsch et al., 2010; Michéa and Komatitsch, 2010). However, ray-based tomographic methods remains the most popular and accessible techniques in mapping the heterogeneous structures of the Earth's interior (e.g. Li et al., 2008; Hung et al., 2011; Tong et al., 2012; Zhao et al., 2012).

As mentioned above, full 3-D numerical simulations in forward modelling and sensitivity kernel calculations guarantee the accuracy of synthetic seismograms and sensitivity kernels for 3-D complex models. But they also make adjoint tomography computationally demanding and even unaffordable. To strike a balance between the computational efficiency and accuracy of full wave-equation based tomographic methods, we propose to conduct the forward modelling and sensitivity kernel calculation in the 2-D source-receiver vertical plane by a high-order finite-difference scheme. As we will show, if only traveltime measurements are considered, this 2-D approximation offers acceptable accuracy. Meanwhile, by numerically solving 2-D wave equations, finite-frequency effects such as wavefront healing are naturally taken into account, and the accuracy of sensitivity kernels in complex heterogeneous models is also improved. Although forward modellings are restricted to 2-D planes, we still plan to invert for 3-D tomographic models on a 3-D inversion grid. The 2-D forwarding modelling and the 3-D tomographic inversion are linked by expressing the model parameters (such as velocity perturbation) at each 2-D forward modelling grid node as a linear interpolation of the model parameters at its surrounding 3-D inversion grid nodes. We name the resultant 2-D-3-D tomographic method as wave-equation based traveltime seismic tomography

SED
6, 2523–2566, 2014

(WETST). Comparing with the 3-D-3-D adjoint tomography based on the spectral element method (Tromp et al., 2005; Fichtner et al., 2006), this 2-D-3-D WETST based upon a 2-D finite-difference scheme is generally more computationally affordable. This also entails that WETST can be applied to tomographic inversions involving significant amount of data based on even moderate computational resources.

Arrival time picking is another important issue for traveltime seismic tomography. Since the early era of ray-based seismic tomography, researchers have mainly relied on manually picked arrival times to map subsurface structures (e.g. Aki and Lee, 1976; Zhao et al., 1992). Arrival times are usually picked within time windows centred at the predicted traveltimes (Kennett and Engdah, 1991; Maggi et al., 2009). In recent years, increasingly number of deployed broadband seismic arrays have resulted in the proliferation of seismic data. To increase efficiency and reduce the amount of manual labour and human errors in seismic data processing, fast and automatic traveltime picking algorithms with high accuracy are highly demanded to process vast amount of seismic recordings. Indeed, various techniques have been presented for automatic/semi-automatic detecting and picking the arrivals of different seismic phases, and the most widely used of which is the short-term-average (STA) to long-term-average (LTA) ratio method and its variations (e.g. Coppens, 1985; Baer and Kradolfer, 1987; Saari, 1991; Earle and Shearer, 1994; Han et al., 2010). Zhang et al. (2003) developed an automatic *P* wave arrival detection and picking algorithm based on the wavelet transform and Akaike information criteria. Cross-correlation method is another routinely used technique to obtain the traveltime anomalies of broadband pulses, which is specially favoured by finite-frequency tomographic applications (e.g. Luo and Schuster, 1991; Dahlen et al., 2000; Tape et al., 2007). However, the quality of picked arrivals by these methods may vary in accuracy for datasets of different signal-to-noise ratio (SNR), and often only arrivals on low-noise seismograms can be effectively picked (Akram, 2011). Specifically, the validity of the correlation-based methods requires that the synthetic seismograms be reasonably similar to the observed seismograms. Less restrictive automatic arrival picking algorithms need to be further developed. In this study, we pro-

SED
6, 2523–2566, 2014

pose two different automatic arrival-time determination methods (Sect. 3) that forms an integral part of our wave-equation based traveltime seismic tomography method.

When arrival-time data and sensitivity kernels are determined or computed, wave-equation based traveltime seismic tomography is cast as an optimization problem. Model parameterization, regularization and methods solving the optimization problem are discussed in Sects. 4 and 5. Finally, examples of sensitivity kernels for different seismic waves are shown in Sect. 6, which provide the basis for future tomographic inversions with various seismic phases. This paper focuses on theoretical derivation of the wave-equation based traveltime seismic tomography. An application of the WETST method is presented in the second paper (Tong et al., 2014b).

2 Tomographic equation

In this section, we set up a linear relationship between the perturbation of arrival time and velocity perturbation in a reference model.

2.1 Traveltime residual

Traveltime seismic tomography generally inverts traveltime residuals of some seismic phases to map the internal Earth structures. A traveltime residual Δt corresponding to the event occurred at $\boldsymbol{x}_s$ and the seismic station located at $\boldsymbol{x}_r$ is written as,

$$\Delta t = T^{\mathrm{obs}} - T^{\mathrm{syn}}, \tag{1}$$

where the observed traveltime T^{obs} is automatically or manually picked on recorded seismogram $d(t)$, and the synthetic arrival time T^{syn} is predicted based on a reference model. In geometrical ray theory, T^{syn} is usually computed by integrating the slowness along a travelling path.

If the corresponding synthetic seismogram $u(t)$ in the reference model is available, the traveltime residual Δt can be approximated by the cross-correlation technique

SED
6, 2523–2566, 2014

(Dahlen et al., 2000)

$$\Delta t \approx \frac{1}{N_r}\int_0^T w(t)\dot{u}(t)[\mathrm{d}(t)-u(t)]\mathrm{d}t, \tag{2}$$

where

$$N_r = \int_0^T w(t)u(t)\ddot{u}(t)\mathrm{d}t$$

and $w(t)$ is a weight function over the time interval $[0,T]$ that can be used to isolate particular seismic phases (Tromp et al., 2005). The accuracy of this approximation improves as data and synthetic pulse becomes more similar, i.e., waveform perturbation $d(t)-u(t)$ in Eq. (2) becomes tiny. Assuming infinitesimal perturbations, Eq. (2) becomes

$$\delta t = \frac{1}{N_r}\int_0^T w(t)\dot{u}(t)\delta u(t)\,\mathrm{d}t, \tag{3}$$

which is used further to set up the relationship between traveltime residual and velocity perturbation.

2.2 Relation between traveltime residual and velocity perturbation

We consider seismic wave propagation in a two-dimensional (2-D) vertical plane which contains the source $\boldsymbol{x}_s$ and the receiver $\boldsymbol{x}_r$. Within this plane, seismic wavefield of a particular phase (without mode conversion) could be assumed to satisfy the 2-D

SED
6, 2523–2566, 2014

acoustic wave equation with initial and boundary conditions,

$$\begin{cases} \frac{\partial^2}{\partial t^2} u(t,\boldsymbol{x}) = \nabla \cdot \left[c^2(\boldsymbol{x}) \nabla u(t,\boldsymbol{x}) \right] + f(t)\delta(\boldsymbol{x} - \boldsymbol{x}_s), \quad \boldsymbol{x} \in S \\ u(0,\boldsymbol{x}) = \partial u(0,\boldsymbol{x})/\partial t = 0, \quad \boldsymbol{x} \in S, \\ \hat{\boldsymbol{n}} \cdot \left[c^2(\boldsymbol{x}) \nabla u(t,\boldsymbol{x}) \right] = 0, \quad \boldsymbol{x} \in \partial S. \end{cases} \tag{4}$$

where $u(t,\boldsymbol{x})$ is the displacement field, $c(\boldsymbol{x})$ is the either P or S wave velocity model, $f(t)$ is the source time function for the point source at $\boldsymbol{x}_s$, and $\hat{\boldsymbol{n}}$ is the normal direction of the boundary ∂S. For a perturbation $\delta c(\boldsymbol{x})$ of the velocity model $c(\boldsymbol{x})$, a consequent perturbed displacement wavefield $\delta u(t,\boldsymbol{x})$ will be generated. In the framework of first-order or Born approximation (e.g. Aki and Richards, 2002; Tromp et al., 2005; Tong et al., 2011), the perturbed wavefield $\delta u(t,\boldsymbol{x})$ is the solution to the following wave equation with subsidiary conditions,

$$\begin{cases} \frac{\partial^2}{\partial t^2} \delta u(t,\boldsymbol{x}) = \nabla \cdot \left[c^2(\boldsymbol{x}) \nabla \delta u(t,\boldsymbol{x}) + 2c(\boldsymbol{x}) \delta c(\boldsymbol{x}) \nabla u(t,\boldsymbol{x}) \right], \quad \boldsymbol{x} \in S, \\ \delta u(0,\boldsymbol{x}) = \partial \delta u(0,\boldsymbol{x})/\partial t = 0, \quad \boldsymbol{x} \in S, \\ \hat{\boldsymbol{n}} \cdot \left[c^2(\boldsymbol{x}) \nabla \delta u(t,\boldsymbol{x}) + 2c(\boldsymbol{x}) \delta c(\boldsymbol{x}) \nabla u(t,\boldsymbol{x}) \right] = 0, \quad \boldsymbol{x} \in \partial S. \end{cases} \tag{5}$$

Multiply an arbitary test function $q(t,\boldsymbol{x})$ on both sides of the first equation in Eq. (5) and then integrate in the surface S and the time interval $[0,T]$, we have

$$\int_0^T \mathrm{d}t \int_S q(t,\boldsymbol{x}) \frac{\partial^2}{\partial t^2} \delta u(t,\boldsymbol{x}) \mathrm{d}\boldsymbol{x} \tag{6}$$

$$= \int_0^T \mathrm{d}t \int_S q(t,\boldsymbol{x}) \nabla \cdot \left[c^2(\boldsymbol{x}) \nabla \delta u(t,\boldsymbol{x}) + 2c(\boldsymbol{x}) \delta c(\boldsymbol{x}) \nabla u(t,\boldsymbol{x}) \right] \mathrm{d}\boldsymbol{x}$$

SED
6, 2523–2566, 2014

which is equal to

$$\int_S \mathrm{d}\boldsymbol{x} \int_0^T \left\{ \frac{\partial}{\partial t} \left[q(t,\boldsymbol{x}) \frac{\partial}{\partial t} \delta u(t,\boldsymbol{x}) - \delta u(t,\boldsymbol{x}) \frac{\partial}{\partial t} q(t,\boldsymbol{x}) \right] + \delta u(t,\boldsymbol{x}) \frac{\partial^2}{\partial t^2} q(t,\boldsymbol{x}) \right\} \mathrm{d}t \tag{7}$$

$$= \int_0^T \mathrm{d}t \int_S \delta u(t,\boldsymbol{x}) \nabla \cdot \left[c^2(\boldsymbol{x}) \nabla q(t,\boldsymbol{x}) \right] \mathrm{d}\boldsymbol{x} - \int_0^T \mathrm{d}t \int_S \nabla \cdot \left[\delta u(t,\boldsymbol{x}) c^2(\boldsymbol{x}) \nabla q(t,\boldsymbol{x}) \right] \mathrm{d}\boldsymbol{x}$$

$$+ \int_0^T \mathrm{d}t \int_S \nabla \cdot \left\{ q(t,\boldsymbol{x}) \left[c^2(\boldsymbol{x}) \nabla \delta u(t,\boldsymbol{x}) + 2c(\boldsymbol{x}) \delta c(\boldsymbol{x}) \nabla u(t,\boldsymbol{x}) \right] \right\} \mathrm{d}\boldsymbol{x}$$

$$- \int_0^T \mathrm{d}t \int_S 2c(\boldsymbol{x}) \delta c(\boldsymbol{x}) \nabla q(t,\boldsymbol{x}) \cdot \nabla u(t,\boldsymbol{x}) \mathrm{d}\boldsymbol{x}.$$

As traveltime residual δt in Eq. (3) is measured at the receiver location $\boldsymbol{x}_\mathrm{r}$, Eq. (3) can be alternatively expressed as

$$\delta t = \frac{1}{N_\mathrm{r}} \int_0^T w(t) \int_S \frac{\partial u(t,\boldsymbol{x})}{\partial t} \delta u(t,\boldsymbol{x}) \delta(\boldsymbol{x} - \boldsymbol{x}_\mathrm{r}) \mathrm{d}\boldsymbol{x} \mathrm{d}t. \tag{8}$$

Sum up Eq. (7) and Eq. (8), use the second and third relationships in Eq. (5), and assume that

$$\begin{cases} \frac{\partial^2}{\partial t^2} q(t,\boldsymbol{x}) - \nabla \cdot \left[c^2(\boldsymbol{x}) \nabla q(t,\boldsymbol{x}) \right] = \frac{1}{N_\mathrm{r}} w(t) \frac{\partial u(t,\boldsymbol{x})}{\partial t} \delta(\boldsymbol{x} - \boldsymbol{x}_\mathrm{r}), \quad \boldsymbol{x} \in S, \\ q(T,\boldsymbol{x}) = \partial q(T,\boldsymbol{x}) / \partial t = 0, \quad \boldsymbol{x} \in S, \\ \hat{\boldsymbol{n}} \cdot c^2(\boldsymbol{x}) \nabla q(t,\boldsymbol{x}) = 0, \quad \boldsymbol{x} \in \partial S, \end{cases} \tag{9}$$

SED
6, 2523–2566, 2014

we can get a relationship as

$$\delta t = -\int_0^T \mathrm{d}t \int_S \left[2c^2(\boldsymbol{x})\nabla q(t,\boldsymbol{x})\cdot\nabla u(t,\boldsymbol{x})\right]\frac{\delta c(\boldsymbol{x})}{c(\boldsymbol{x})}\mathrm{d}\boldsymbol{x}. \tag{10}$$

By defining the traveltime sensitivity kernel

$$K(\boldsymbol{x};\boldsymbol{x}_\mathrm{r},\boldsymbol{x}_\mathrm{s}) = -\int_0^T \left[2c^2(\boldsymbol{x})\nabla q(t,\boldsymbol{x})\cdot\nabla u(t,\boldsymbol{x})\right]\mathrm{d}t, \tag{11}$$

Equation (10) provides a concise mathematical expression of the relationship between traveltime residual δt and relative velocity perturbation $\delta c(\boldsymbol{x})/c(\boldsymbol{x})$

$$\delta t = \int_\Omega K(\boldsymbol{x};\boldsymbol{x}_\mathrm{r},\boldsymbol{x}_\mathrm{s})\frac{\delta c(\boldsymbol{x})}{c(\boldsymbol{x})}\mathrm{d}\boldsymbol{x}. \tag{12}$$

The traveltime kernel $K(\boldsymbol{x};\boldsymbol{x}_\mathrm{r},\boldsymbol{x}_\mathrm{s})$ is a weighted convolution of forward wavefield gradient $\nabla u(t,\boldsymbol{x})$ and the adjoint wavefield gradient $\nabla q(t,\boldsymbol{x})$, which can be obtained by solving two wave Eqs. (4) and (9). Assume small perturbations, we can set that Δt in Eq. (1) is equal to δt, and Eq. (12) becomes

$$T^{\mathrm{obs}} - T^{\mathrm{syn}} = \int_\Omega K(\boldsymbol{x};\boldsymbol{x}_\mathrm{r},\boldsymbol{x}_\mathrm{s})\frac{\delta c(\boldsymbol{x})}{c(\boldsymbol{x})}\mathrm{d}\boldsymbol{x}. \tag{13}$$

We call relation (13) the *tomographic equation* of wave-equation based traveltime seismic tomography. Once the observed arrival time T^{obs} and synthetic arrival time T^{syn} are measured or calculated, tomographic equation (13) can be inverted to infer the relative velocity perturbation $\delta c(\boldsymbol{x})/c(\boldsymbol{x})$.

SED
6, 2523–2566, 2014

3 Arrival time picking

We first discuss how to pick the arrival times of a particular seismic phase on observed and synthetic seismograms, i.e., T^{obs} and T^{syn} in Eq. (13). Since any errors in arrival times will distort the velocity anomalies, this step is crucial for traveltime seismic tomography. Although manual arrival-picking is time-consuming and labour intensive, it is still one of the most reliable and stable techniques to determine the arrival times of specific seismic phases on observed seismograms. For example, the first-arrivals picked by analysts of the combined seismic network in Japan (known as the JMA Unified Catalogue) have the accuracies of about 0.1 s for P arrival and 0.1–0.2 s for S arrival (Tong et al., 2012). Before the advent of an automatic, accurate and robust arrival time picking method for data, we prefer to use manually picked arrival times T^{obs} on observed seismograms for tomographic inversion purpose.

Regarding to the arrival time T^{syn} of a particular phase on synthetic seismograms, we could also use manual picking. But extra subjective errors will be introduced into the traveltime residual Δt and further affect final tomographic results. Since synthetic seismograms are generated by numerical methods, the errors come mainly from numerical dispersion and can be controlled (but can not be avoided) by employing accurate forward solver or fine meshes in forward numerical modelling. For low-noise seismograms, automatic time-picking schemes such as the STA/LTA method have been proved to be accurate and efficient for detecting the arrivals of different seismic phases (e.g. Saari, 1991; Han et al., 2010). In this study, we present a new envelope energy ratio method to pick up the arrival times on synthetic seismograms, which has a better performance than the STA/LTA method. On the other hand, if the starting model $\boldsymbol{m}_0$ for a tomographic inversion has (or is near) a simple geometry where travelling paths can be easily and accurately determined, the combined ray and cross-correlation method developed later can be used to obtain arrival times of particular phases on synthetic seismograms.

SED
6, 2523–2566, 2014

3.1 Envelop energy ratio method

We give a brief introduction to the STA/LTA method and then discuss the envelop energy ratio (EER) method, which is an improved version of the STA/LTA algorithm. Let $u(t)$ represent a seismogram with a dominant period of T_0 in the time window $[0,T]$, then the average energies in the short and long term windows preceding the time t are defined as

$$S(t) = \frac{1}{\alpha T_0}\int_{t-\alpha T_0}^{t} u^2(\tau)\mathrm{d}\tau, \quad L(t) = \frac{1}{\beta T_0}\int_{t-\beta T_0}^{t} u^2(\tau)\mathrm{d}\tau, \tag{14}$$

where $t \in [0,T]$ and $0 < \alpha < \beta$ are coefficients determining the lengths of the short and long term time windows and should be determined by the user. Usually, α and β are chosen to be $2 \le \alpha \le 3$ and $5 \le \beta \le 10$, respectively (Earle and Shearer, 1994). $u(\tau)$ is assumed to be zero for $\tau < 0$. Define the ratio

$$R(t) = \frac{S(t)}{L(t)}, \tag{15}$$

and if the ratio $R(t)$ first exceeds a user-defined threshold at t_0, t_0 is considered to be the approximate onset time of first arrival on the seismogram $u(t)$ (Munro, 2004). It is also claimed that the maximum value of the derivative $\mathrm{d}R(t)/\mathrm{d}t$ may be closer to the break time of the first arrival (Wong et al., 2009).

In addition, the envelop function of seismogram $e(t) = |u(t) + iH[u(t)]|$, where $H[u(t)]$ denotes the Hilbert transform of $u(t)$, can be also used in seismic data analysis (e.g. Baer and Kradolfer, 1987; Maggi et al., 2009). Since the envelope function remains positive at zero crossings among different phase arrivals, average energy taken from an envelope function may be a better measure of the signal strength (Baer and Kradolfer, 1987; Earle and Shearer, 1994). Meanwhile, Wong et al. (2009) proposed the modified energy method which has excellent performance in determining the break time of first arrival. By incorporating the envelope function and the modified energy method (Wong et al., 2009), we define the following envelop energy ratio function to determine the

SED
6, 2523–2566, 2014

arrival time of an interested seismic phase filtered by the window function $w(t)$

$$r(t) = \frac{\int_{t-\beta T_0}^{t+\alpha T_0} w(\tau) e^2(\tau) \mathrm{d}\tau}{\int_{t-\gamma T_0}^{t} w(\tau) e^2(\tau) \mathrm{d}\tau}, \tag{16}$$

where $\alpha \geq 0$ and $\beta \geq \gamma \geq 1$. The peak of the ratio function $r(t)$ is very close to the onset time of the interested seismic phase.

To show the performance of the EER method, we apply it to shear-wave synthetic seismograms generated by an earthquake at 12.0 km depth in a homogeneous crust with a thickness of 30.0 km based on a high-order finite-difference method (in Appendix). 51 surface stations with an equal spacing of 2.0 km are used to record seismograms. $\alpha = \beta = \gamma = 1.0$ are chosen in formula (16). Figure 1a–c shows the S wave arrival-time picking using the STA/LTA and EER methods on the seismogram for trace number 26 (Fig. 1d). We can see that S arrival time determined by the EER method is very close to the theoretical arrival time with errors smaller than 0.05 s. For the STA/LTA method, the threshold value is set to be 1.0×10^{-8}, and the obtained S arrival time is 0.24 s later than the theoretical arrival time. Note that an error of 0.24 s is unacceptable in traveltime inversion for local structures. We further show S and SmS arrival times on all 51 seismograms in Fig. 1d. For direct S wave, results of both STA/LTA and EER methods are relatively close to the theoretical arrival times, with errors around 0.3 s and less than 0.1 s, respectively. However, for SmS phase, the STA/LTA algorithm is not able to give accurate estimates on the breaking times. In comparison, the EER method gives picked arrivals with accuracy similar to the direct S wave case, and 70 % of the errors are still less than 0.1 s. We have fixed all parameters for the STA/LTA and EER methods in picking the S and SmS arrival times. Actually, the accuracy of time picking on any single seismogram can be improved by slightly tuning some parameters, such as the threshold value for the STA/LTA method and the lengths of the time windows for both methods. We also find that the accuracy of the STA/LTA method is very sensitive to the threshold value and it is not an easy task to determine an appropri-

SED
6, 2523–2566, 2014

ate threshold in practice. For the EER method, however, it is simple to locate the peak of the ratio function $r(t)$. This implies that the EER method could be a better choice for arrival-time picking on synthetic seismograms.

3.2 Combined ray and cross-correlation method

Because of the non-linearity of seismic inverse problems, seismic tomography usually relies on an iterative method to find the optimal model. If the starting model $\boldsymbol{m}_0$ for traveltime seismic tomography is simple (e.g., 1-D layered model) and travelling paths of particular phases can be easily traced, the arrival times T_0^{syn} of synthetics in $\boldsymbol{m}_0$ can be accurately determined based on ray theory. Meanwhile, we may expect that synthetic seismograms in the $(i+1)$th model $\boldsymbol{m}_{i+1}$ are reasonably similar to those in the ith model $\boldsymbol{m}_i$ $(i \geq 0)$, and the arrival-time shift $\delta t_{i+1,i}$ of a particular phase in models $\boldsymbol{m}_{i+1}$ and $\boldsymbol{m}_i$ can be calculated with high accuracy by maximizing the cross-correlation formula,

$$\max_{\delta t_{i+1,i}} \frac{\int_0^T w(\tau) s(\tau; \boldsymbol{m}_{i+1}) s(\tau - \delta t_{i+1,i}; \boldsymbol{m}_i) \mathrm{d}\tau}{\left[\int_0^T w(\tau) s^2(\tau; \boldsymbol{m}_{i+1}) \mathrm{d}\tau \int_0^T s^2(\tau - \delta t_{i+1,i}; \boldsymbol{m}_i) \mathrm{d}\tau\right]^{1/2}}, \tag{17}$$

where $w(t)$ is the time window function used to isolate the interested phase (Liu et al., 2004). Consequently, the arrival time T_{i+1}^{syn} of the synthetic seismogram in model $\boldsymbol{m}_{i+1}$ satisfies the following relation,

$$T_{i+1}^{\mathrm{syn}} = T_0^{\mathrm{syn}} + \sum_{j=0}^{i} \delta t_{j+1,j}. \tag{18}$$

Since T_0^{syn} and $\delta t_{j+1,j}$ are calculated with ray theory and cross-correlation method, respectively, Eq. (18) is called the combined ray and cross-correlation method.

Continuing the numerical example shown in the section of the EER method, we intend to verify the validity of the combined ray and cross-correlation method. Let $\boldsymbol{m}_0$

SED
6, 2523–2566, 2014

be the crust model with an S wave velocity of 3.2 km s^{-1} and a thickness of 30.0 km. S wave velocity in $\boldsymbol{m}_1$ is assumed to be 3.456 km s^{-1} which has a perturbation of 8.0 % with respect to $\boldsymbol{m}_0$. Synthetic seismograms generated by an earthquake at 12.0 km depth are calculated and recorded by 51 stations at the surface in both $\boldsymbol{m}_0$ and $\boldsymbol{m}_1$. For models $\boldsymbol{m}_0$ and $\boldsymbol{m}_1$, theoretical arrival times of S and SmS phases at each station can be calculated based on the ray theory (see solid red circles and black squares in Fig. 2a). Based on Eq. (17), we also measure arrival shifts of S and SmS in $\boldsymbol{m}_1$ from those in $\boldsymbol{m}_0$. Adding S and SmS arrival shifts to their corresponding arrival times for $\boldsymbol{m}_0$ (solid black squares in Fig. 2a), we get the approximated arrival times of S and SmS in model $\boldsymbol{m}_1$ (blue stars in Fig. 2a). Figure 2b shows the errors of the combined ray and cross-correlation method in determining the arrival times of S and SmS in model $\boldsymbol{m}_1$. It can be observed that the errors of direct S arrivals are less than 0.005 s, and 70 % errors of the SmS phases are smaller than 0.005 s with maximum error around about 0.175 s occurring at the 4th and 48th stations. Considering that the traveltime differences of the SmS phase in the two models are about 1.7 s at the two stations, these picking errors are relatively small. This numerical example suggests that the combined ray and cross-correlation method could serve as an efficient tool for high accuracy arrival-time picking on synthetic seismograms in the iterative wave-equation based tomographic inversions.

4 Model Parameterization

Tomographic equation (13) needs invariably to be discretized for actual inversions (Nolet et al., 2005). This gives rise to model parameterization, which is an approximation to the true Earth structure. Model parameterization determines the accuracy of forward modelling and hence affects the final form of tomographic inversion results. Most commonly, functional approach with a set of basis functions or an a prior functional form, such as cells and grid nodes have been adopted to represent the Earth structure (e.g. Dziewonski, 1984; Aki and Lee, 1976; Thurber, 1983). Each approach has its own

SED
6, 2523–2566, 2014

advantages and drawbacks (e.g. Zhao, 2009; Rawlinson et al., 2010). To guarantee accurate computation of synthetic seismograms and traveltime kernels and to adapt to local variations in data coverage, we use two sets of grid nodes (i.e., forward modelling grid and inversion grid) to parameterize the Earth structure for forward modelling and inversion algorithms in this study.

4.1 Forward modelling grid

As discussed in Sect. 2, we need to solve wave Eqs. (4) and (9) to obtain synthetic seismogram $u(t)$ and traveltime kernel $K(\boldsymbol{x})$. Many numerical methods such as staggered-grid finite-difference (FD) method (e.g. Virieux, 1984; Graves, 1996) and spectral-element method (Komatitsch and Tromp, 1999) are well suited for this kind of forward modelling. In this study, we choose a FD scheme called high-order central difference method (see Appendix) to conduct forward modelling. The prominent feature of this high-order central difference method is that it simultaneously computes the displacement $u(t,\boldsymbol{x})$ and the spatial gradient field $\nabla u(t,\boldsymbol{x})$, making the computation of the traveltime kernel $K(\boldsymbol{x})$ very straightforward. It is also easier to implement the high-order central difference method than the staggered-grid finite-difference (FD) method and spectral-element method. When sensitivity kernels are calculated by solving the full wave equation, there are spurious amplitudes in the immediate vicinity of the sources and receivers (Tape et al., 2007; Tong et al., 2014a). An efficient way of removing these spurious amplitudes is to smooth the traveltime kernel $K(\boldsymbol{x}) = K(x,z)$ with a 2-D Gaussian

$$G(x,z) = \frac{4}{\pi\sigma^2} e^{-4(x^2+z^2)/\sigma^2}, \tag{19}$$

where σ is the averaging scale length chosen to be less than the main wavelength of the seismic waves (Tape et al., 2007). The smoothed traveltime kernel $\tilde{K}(x,z)$ is given

SED
6, 2523–2566, 2014

by

$$\tilde{K}(x,z) = \iint_S K(x-x',z-z')G(x',z')\mathrm{d}x'\mathrm{d}z', \tag{20}$$

i.e., the smoothed kernel value at a given point is obtained by averaging the unsmoothed kernel values at its neighbouring points.

For the 2-D FD numerical simulation, the continuous area S is sampled by a set of n discrete nodes $\boldsymbol{x}_i$ $(i = 1,2,\cdots,n)$. By choosing a corresponding set of n basis functions $L_i(\boldsymbol{x})$ $(i = 1,2,\cdots,n)$, the smoothed traveltime kernel $\tilde{K}(\boldsymbol{x})$ and the relative velocity perturbation $\delta c(\boldsymbol{x})/c(\boldsymbol{x})$ can be expanded into linear combinations of the basis functions as

$$\tilde{K}(\boldsymbol{x};\boldsymbol{x}_\mathrm{r},\boldsymbol{x}_\mathrm{s}) = \sum_{i=1}^{n} K_i L_i(\boldsymbol{x}), \quad \delta c(\boldsymbol{x})/c(\boldsymbol{x}) = \sum_{i=1}^{n} C_i L_i(\boldsymbol{x}), \tag{21}$$

where K_i and C_i are the corresponding coefficients related to the basis function $L_i(\boldsymbol{x})$. Substituting Eq. (21) into Eq. (13) results in the discrete form of the tomographic equation

$$T^{\mathrm{obs}} - T^{\mathrm{syn}} = \int_S \left[\sum_{j=1}^{n} K_j L_j(\boldsymbol{x})\right]\left[\sum_{i=1}^{n} C_i L_i(\boldsymbol{x})\right]\mathrm{d}\boldsymbol{x} = \sum_{i=1}^{n}\left[\sum_{j=1}^{n} K_j \int_\Omega L_j(\boldsymbol{x})L_i(\boldsymbol{x})\mathrm{d}\boldsymbol{x}\right] C_i. \tag{22}$$

A general way to define a basis function $L_i(\boldsymbol{x})$ is to construct a local interpolation function on knot node $\boldsymbol{x}_i$ and its neighbours. The possibility of different choices for the basis functions $L_i(\boldsymbol{x})$ $(i = 1,\cdots,n)$ has led to various inversion algorithms (Nolet et al., 2005). As the high-order central difference method discussed in this study simulates seismic wave propagation on a 2-D regular mesh, we assume the spatial increments along x and z directions are Δx and Δz, respectively. Let the knot node $\boldsymbol{x}_i$ with a global index i

SED
6, 2523–2566, 2014

be the grid node (x_m, z_n) on the 2-D mesh. In this scenario, the simplest basis function may be the piecewise constant function

$$L_i(\boldsymbol{x}) = L_i(x,z) = \begin{cases} 1, & \text{if } (x,z) \in \left[x_{m-1/2}, x_{m+1/2}\right] \times \left[z_{n-1/2}, z_{n+1/2}\right]; \\ 0, & \text{else .} \end{cases} \tag{23}$$

And the coefficient of the unknown C_i in Eq. (22) is

$$\sum_{j=1}^{n} K_j \int_{\Omega} L_j(\boldsymbol{x}) L_i(\boldsymbol{x}) \mathrm{d}\boldsymbol{x} = \Delta x \Delta z K_i. \tag{24}$$

However, interpolation function with the basis functions (23) is not even continuous. To make the interpolation function continuous, we could use bilinear interpolation to fit the perturbation field $\delta c(\boldsymbol{x})/c(\boldsymbol{x})$ and the traveltime kernel $K(\boldsymbol{x})$. Bilinear interpolation performs linear interpolation first in one direction and then in the other direction. The basis function $L_i(\boldsymbol{x})$ for bilinear interpolation takes the following form

$$L_i(\boldsymbol{x}) = L_i(x,z) = \begin{cases} \frac{x-x_{m-1}}{x_m-x_{m-1}} \frac{z-z_{n-1}}{z_n-z_{n-1}}, & \text{if } (x,z) \in \left[x_{m-1}, x_m\right] \times \left[z_{n-1}, z_n\right]; \\ \frac{x-x_{m-1}}{x_m-x_{m-1}} \frac{z_{n+1}-z}{z_{n+1}-z_n}, & \text{if } (x,z) \in \left[x_{m-1}, x_m\right] \times [z_n, z_{n+1}]; \\ \frac{x_{m+1}-x}{x_{m+1}-x_m} \frac{z-z_{n-1}}{z_n-z_{n-1}}, & \text{if } (x,z) \in [x_m, x_{m+1}] \times \left[z_{n-1}, z_n\right]; \\ \frac{x_{m+1}-x}{x_{m+1}-x_m} \frac{z_{n+1}-z}{z_{n+1}-z_n}, & \text{if } (x,z) \in [x_m, x_{m+1}] \times [z_n, z_{n+1}]; \\ 0, & \text{else .} \end{cases} \tag{25}$$

Correspondingly, the coefficient for the unknown C_i in Eq. (22) becomes

$$\sum_{j=1}^{n} K_j \int_{\Omega} L_j(\boldsymbol{x}) L_i(\boldsymbol{x}) \mathrm{d}\boldsymbol{x} = \Delta x \Delta z \begin{pmatrix} \frac{1}{36} & \frac{4}{36} & \frac{1}{36} \\ \frac{4}{36} & \frac{16}{36} & \frac{4}{36} \\ \frac{1}{36} & \frac{4}{36} & \frac{1}{36} \end{pmatrix} \circ \begin{pmatrix} K_{m-1,n+1} & K_{m,n+1} & K_{m+1,n+1} \\ K_{m-1,n} & K_{m,n} & K_{m+1,n} \\ K_{m-1,n-1} & K_{m,n-1} & K_{m+1,n-1} \end{pmatrix}, \tag{26}$$

SED
6, 2523–2566, 2014

where $\circ$ denotes entrywise product and kernel values for global and local grids are linked by $K_{i+pM+q} = K_{m+p,n+q}$ (M is the number of grid nodes along x direction, and $p,q = -1,0,1$). To have a smoother fitting function, we could further use bicubic interpolation, which is an extension of cubit interpolation on 2-D regular mesh. Actually, in the framework of piecewise constant interpolation (Eq. 23), both bilinear interpolation and bicubic interpolation can be achieved by replacing C_i's coefficient $\Delta x \Delta z K_i$ in Eq. (24) with a weighted average value $\Delta x \Delta z \tilde{K}_i$ around the knot node $\boldsymbol{x}_i$ and its neighbours such as shown in Eq. (26). Since we have previously smoothed the kernel by convolving it with a Gaussian, using piecewise constant interpolation or bilinear interpolation to construct tomographic equation (22) is accurate enough for practical applications.

4.2 Inversion grid

For the high-order central difference scheme, we assume that seismic waves propagate in 2-D vertical planes and hence sensitivity kernels are restricted to the same 2-D planes. For a single pair of source $\boldsymbol{x}_s$ and receiver $\boldsymbol{x}_r$, the forward grid nodes and equally the velocity model parameters C_i are distributed on a 2-D regular mesh in Eq. (22). An additional set of grid nodes needs to be introduced to characterize the actual 3-D tomographic region. For simplicity, we use a regular grid with variable grid intervals to represent the final tomographic results, which has the advantage of allowing a fine grid for a target volume with dense data coverage (mostly depending on spatial distribution of source and receivers) to be imbedded in coarse grid nodes.

To be consistent with the realistic application in the second paper, we directly set up the inversion grid in geographical coordinate system (d,ϕ,λ), where d, ϕ, and λ are depth, latitude and longitude, respectively. If the Cartesian coordinate system is adopted for the inversion grid, the following derivation procedure is almost the same. In a 3-D regular inversion grid, each forward modelling grid node $\boldsymbol{x}_i$ ($i = 1,2,\cdots,n$) is located within a cube formed by eight inversion grid nodes (Fig. 3). It is natural and straightforward to use trilinear interpolation between the eight grid nodes (Zhao et al., 1992). Note that the Cartesian coordinate $\boldsymbol{x}_i$ should be transformed into geographical

SED
6, 2523–2566, 2014

coordinate $\tilde{\boldsymbol{x}}_i$ prior to locating it in a cube. Assume that $\tilde{\boldsymbol{x}}_i$ is located within the cube formed by $(d_{r+j_1}, \phi_{p+j_2}, \lambda_{q+j_3})$ $(j_1, j_2, j_3 = 0, 1; 1 \le r+j_1 \le R; 1 \le p+j_2 \le P; 1 \le q+j_3 \le Q$; R, P, Q are the numbers of inversion grid nodes along depth, latitude and longitude, respectively), the unknown velocity model parameter C_i corresponding to $\tilde{\boldsymbol{x}}_i$ can be expressed as a linear combination of the parameters $X_{r+j_1,p+j_2,q+j_3}$ $(j_1, j_2, j_3 = 0, 1)$ at the eight inversion grid nodes:

$$C_i = \sum_{j_1,j_2,j_3=0}^{1} \left(1 - \left|\frac{d - d_{r+j_1}}{d_{r+1} - d_r}\right|\right)\left(1 - \left|\frac{\phi - \phi_{p+j_2}}{\phi_{p+1} - \phi_p}\right|\right)\left(1 - \left|\frac{\psi - \psi_{q+j_3}}{\psi_{q+1} - \psi_q}\right|\right) X_{r+j_1,p+j_2,q+j_3}, \tag{27}$$

and defines a continuously varying velocity perturbation field $\delta c(\boldsymbol{x})/c(\boldsymbol{x})$. Note that the velocity field $c(\boldsymbol{x})$ itself can be discontinuous. Substituting Eq. (27) into Eq. (22) gives the tomographic equation on the inversion grid

$$T^{\text{obs}} - T^{\text{syn}} = \sum_{r=1}^{R}\sum_{p=1}^{P}\sum_{q=1}^{Q} a_{r,p,q} X_{r,p,q}, \tag{28}$$

where $a_{r,p,q}$ is the coefficient for the unknown $X_{r,p,q}$ and pre-determined, the accuracy of which relies on not only the accurate calculation of the traveltime kernel $K(\boldsymbol{x})$ but also the choice of the inversion grid. For the convenience of discussion, we convert the 3-D array index (r, p, q) of the inversion grid to 1-D index $n = (r-1)PQ + (q-1)P + q$ $(1 \le n \le N = RPQ)$. Tomographic equation (28) can be rewritten as

$$T^{\text{obs}} - T^{\text{syn}} = \sum_{n=1}^{N} a_n X_n \tag{29}$$

for a single pair of source $\boldsymbol{x}_s$ and receiver $\boldsymbol{x}_r$, which relates the traveltime residual $T^{\text{obs}} - T^{\text{syn}}$ linearly to the unknown relative velocity perturbation X_n $(1 \le n \le N)$ on the inversion grid.

SED
6, 2523–2566, 2014

5 Regularization and Inversion Method

With a significant increase in both quantity and quality of seismic data from the proliferation of dense seismic arrays, increasing number of seismic data will be involved in seismic tomography, which may result in higher-resolution tomographic models. Certainly, more data will increase the complexity of seismic inverse problem.

When M seismic measurements are used to explore the subsurface structure, M tomographic equations take the form of Eq. (29) and form a linear system $\boldsymbol{b} = \mathbf{A}\boldsymbol{X}$ at each iteration, where $\boldsymbol{b} = [b_m]_{M\times 1}$ and $b_m = T_m^{\mathrm{obs}} - T_m^{\mathrm{syn}}$ is the iterative traveltime residual vector, $\mathbf{A} = [a_{m,n}]_{M\times N}$ is the Fréchet or Jacobin matrix calculated in the current iterative model and $\boldsymbol{X} = [X_n]_{N\times 1}$ is the unknown model vector. Since the problem $\boldsymbol{b} = \mathbf{A}\boldsymbol{X}$ is always ill-posed (either because of non-uniqueness or non-existence of $\boldsymbol{X}$), the general way to solve it is to seek a solution that minimizes the following regularized objective function

$$\chi(\boldsymbol{X}) = \frac{1}{2}(\mathbf{A}\boldsymbol{X} - \boldsymbol{b})^T \mathbf{C}_{\mathrm{d}}^{-1}(\mathbf{A}\boldsymbol{X} - \boldsymbol{b}) + \frac{\epsilon^2}{2}\boldsymbol{X}^T\mathbf{C}_{\mathrm{m}}^{-1}\boldsymbol{X} + \frac{\eta^2}{2}\boldsymbol{X}^T\mathbf{D}^T\mathbf{D}\boldsymbol{X}, \tag{30}$$

where $\mathbf{C}_{\mathrm{d}}$ and $\mathbf{C}_{\mathrm{m}}$ are the a prior data and model covariance matrix which reflect the uncertainties in the data and the initial model (Rawlinson et al., 2010), $\mathbf{D}$ is a derivative smoothing operator for model vector $\boldsymbol{X}$, ϵ and η are the damping parameter and smoothing parameter, respectively (e.g. Tarantola, 2005; Li et al., 2008; Rawlinson et al., 2010). The last two terms on the right hand side of Eq. (30) are regularization terms, which are included to improve the conditioning of the inverse problem $\boldsymbol{b} = \mathbf{A}\boldsymbol{X}$ and are designed to give preference to solutions with desirable properties (Aster et al., 2012): damping favours a result that is close to the reference model, while smoothing reduces the differences between adjacent nodes and thus produces smooth model variations (Li et al., 2006). Generally speaking, objective function (30) tries to strike a balance between how well the solution satisfies the data, the variations of the solution from the reference model, and the smoothness of the solution model.

SED
6, 2523–2566, 2014

Calculating the gradient (Fréchet derivative) of the objective function $\chi(\boldsymbol{X})$ is often a key step in finding an optimal solution to the minimization problem (30) (Rawlinson et al., 2010). Here the Fréchet derivative of the objective function $\chi(\boldsymbol{X})$ can be expressed as

$$\frac{\partial \chi(\boldsymbol{X})}{\partial \boldsymbol{X}} = \left(\mathbf{A}^T \mathbf{C}_{\mathrm{d}}^{-1} \mathbf{A} + \epsilon^2 \mathbf{C}_{\mathrm{m}}^{-1} + \eta^2 \mathbf{D}^T \mathbf{D}\right) \boldsymbol{X} - \mathbf{A}^T \mathbf{C}_{\mathrm{d}}^{-1} \boldsymbol{b}. \tag{31}$$

Based on the Fréchet derivative $\partial \chi(\boldsymbol{X})/\partial \boldsymbol{X}$, we describe two different approaches to solve the optimization (minimization) problem (Eq. 30).

5.1 LSQR solver

The minimizer $\tilde{\boldsymbol{X}}$ of Eq. (30) satisfies $\partial \chi(\tilde{\boldsymbol{X}})/\partial \boldsymbol{X} = 0$ and formally can be expressed as

$$\tilde{\boldsymbol{X}} = \left(\mathbf{A}^T \mathbf{C}_d^{-1} \mathbf{A} + \epsilon^2 \mathbf{C}_m^{-1} + \eta^2 \mathbf{D}^T \mathbf{D}\right)^{-1} \mathbf{A}^T \mathbf{C}_d^{-1} \boldsymbol{b}. \tag{32}$$

Clearly, to explicitly obtain $\tilde{\boldsymbol{X}}$ we need to invert an $N \times N$ matrix. There are various methods available to fulfil this goal, such as LU decomposition, single value decomposition (SVD), conjugate-gradient type of methods such as LSQR algorithm. Among these methods, LSQR algorithm may be one of the most efficient and widely used methods to solve a linear system, especially when N is very large (Paige and Saunders, 1982). Additionally, the minimization problem (Eq. 30) is equivalent to solving the following linear system in a least square sense

$$\begin{pmatrix} \mathbf{C}_d^{-1/2} \mathbf{A} \\ \epsilon \mathbf{C}_m^{-1/2} \\ \eta \mathbf{D} \end{pmatrix} \boldsymbol{X} = \begin{pmatrix} \mathbf{C}_d^{-1/2} \boldsymbol{b} \\ \mathbf{0} \\ \mathbf{0} \end{pmatrix}, \tag{33}$$

and application of LSQR or SVD to Eq. (33) will give the same solution as that of Eq. (32) (Rawlinson et al., 2010). Once we obtain a perturbation velocity field $\tilde{\boldsymbol{X}}$, the velocity

SED
6, 2523–2566, 2014

model can be updated from the current velocity model on inversion grid, C, to $C + \tilde{\boldsymbol{X}}$. Because of the non-linearity of the inverse problem, further iteration may be needed to update the velocity model until the objective function $\chi(\boldsymbol{X})$ reaches below a tolerance level.

5.2 Non-linear conjugate gradient method

Once we have the Fréchet derivative of the objective function computed in Eq. (31), instead of inverting the matrix in Eq. (32), we can alternatively use a non-linear conjugate-gradient method to iteratively improve the model (e.g. Fletcher and Reeves, 1964; Tromp et al., 2005). Previous studies have shown the feasibility and efficiency of this non-linear conjugate-gradient method in recovering seismic properties of the Earth interior (e.g. Tape et al., 2007, 2009; Zhu et al., 2012). Here we summarize the step-by-step process of this non-linear conjugate-gradient method, which starts from $k = 0$ (Tape et al., 2007; Kim et al., 2011):

1. Calculate the objective function $\chi(\boldsymbol{X}^k)$, compute the gradient $\boldsymbol{g}^k = \partial\chi/\partial\boldsymbol{X}^k$,
2. Compute the model update direction $\boldsymbol{p}^k = -\boldsymbol{g}^k + \beta_k \boldsymbol{p}^{k-1}$. For the first iteration $k = 0$, set $\beta_0 = 0$ and $\boldsymbol{p}^0 = -\boldsymbol{g}^0$; otherwise calculate β_k based on the formula

$$\beta_k = \max\left(0, \frac{\boldsymbol{g}^k \cdot (\boldsymbol{g}^k - \boldsymbol{g}^{k-1})}{\boldsymbol{g}^{k-1} \cdot \boldsymbol{g}^{k-1}}\right). \tag{34}$$

3. Determine the step length λ_k in the model update direction:
   - Let $f_1 = \chi(\boldsymbol{X}^k)$, $g_1 = \boldsymbol{g}^k \cdot \boldsymbol{p}^k$, and compute a test step length $\lambda_t = -2f_1/g_1$.
   - Calculate the test perturbation model $\boldsymbol{X}_t^k = \boldsymbol{X}^k + \lambda_t \boldsymbol{p}^k$.
   - Compute the objective function $\chi(\boldsymbol{X}_t^k)$ and let $f_2 = \chi(\boldsymbol{X}_t^k)$. Note that we generally have $f_1 > f_2 > 0$.

SED
6, 2523–2566, 2014

– Compute

$$\gamma = [(f_2 - f_1) - g_1\lambda_t]/\lambda_t^2, \quad \xi = g_1 \tag{35}$$

and then λ_k is given by

$$\lambda_k = \begin{cases} -\xi/(2\gamma), & \gamma \neq 0; \\ \text{error}, & \text{otherwise.} \end{cases} \tag{36}$$

4. Update the perturbation model $\boldsymbol{X}^{k+1} = \boldsymbol{X}^k + \lambda_k \boldsymbol{p}^k$.

5. If $\|\boldsymbol{g}^k\|_{L_2} = (\boldsymbol{g}^k \cdot \boldsymbol{g}^k)^{1/2} \leq \epsilon$, the tolerance level, then $\boldsymbol{X}^{k+1}$ is the optimal perturbation model; otherwise reiterate from the first step (i) with $k + 1$.

For the current model $\boldsymbol{m}_k$ which has a perturbation $\boldsymbol{X}^k$ from the starting model $\boldsymbol{m}_0$, we can rewrite the gradient of the objective function as

$$\frac{\partial \chi(\boldsymbol{X}^k)}{\partial \boldsymbol{X}} = -(\mathbf{A}^k)^T \mathbf{C}_d^{-1} \boldsymbol{b}^k + \left(\epsilon^2 \mathbf{C}_m^{-1} + \eta^2 \mathbf{D}^T \mathbf{D}\right) \boldsymbol{X}^k, \tag{37}$$

where $\mathbf{A}^k$ and $\boldsymbol{b}^k$ are respectively the Fréchet matrix and traveltime residuals in the kth model. The first term on the right hand side of Eq. (37) is actually the sum of all traveltime kernels (negatively) weighted by their corresponding traveltime residuals. That is to say, if no damping and smoothing operations are applied, the gradient (Eq. 37) is simply the sum of all weighted individual traveltime kernels. Since operators $\mathbf{C}_d^{-1}$, $\mathbf{C}_m^{-1}$ and $\mathbf{D}$ remain constant throughout the whole process, to update the model from $\boldsymbol{m}_k$ to $\boldsymbol{m}_{k+1}$ we only need to compute the Fréchet matrix and traveltime residuals in model $\boldsymbol{m}_k$. This is different from the approach using the LSQR algorithm as a linear system is solved at each iteration. Generally speaking, the model update with the LSQR algorithm may be larger than the non-linear conjugate-gradient method and the LSQR approach probably requires fewer iterations.

SED
6, 2523–2566, 2014

6 Numerical examples

As discussed in Sect. 5, computing traveltime sensitivity kernel or the Fréchet derivative of the objective function is one of the key components of wave-equation based traveltime seismic tomography. In this section, we show examples of Fréchet kernel for one earthquake. These examples provide insights into sensitivities of various seismic phases and the future applications of wave-equation based traveltime seismic tomography involving tens of thousands of seismic records.

A two-layer S wave velocity model with the Moho discontinuity at a depth of 30.0 km is used as a reference model. The size of the model is 100 km × 50 km. S wave velocities in the crust and the mantle are $3.2\,\mathrm{km\,s^{-1}}$ and $4.5\,\mathrm{km\,s^{-1}}$, respectively. The "true" model is the same two-layer S wave velocity model but with a −5.0 % low velocity anomaly (red box in Fig. 5) and a +5.0 % high velocity anomaly (blue box in Fig. 5) included in the mid-crust. An earthquake is placed at the horizontal distance $x = 50.0\,\mathrm{km}$ and the depth of 12.0 km with the dominant frequency of the Gaussian source time function at 1.0 Hz. There are 51 stations equally spaced on the surface with an interval of 2.0 km. The high-order central difference method is used as the forward solver. Seismograms recorded at $x = 14.0\,\mathrm{km}$ and $x = 86.0\,\mathrm{km}$ on the surface are shown in Fig. 4a and 4b, respectively. Three main phases can be observed in these seismograms, including the direct S wave, the Moho reflected phase SmS and the surface reflected wave sSmS, which provide complementary information on the crustal structures. For example, D. Zhao et al. (2005) have used S, SmS and sSmS arrivals to conduct crustal tomography in the 1992 Landers earthquake area with a ray-based tomographic method. Here we compute Fréchet kernels for the three seismic phases. Because only sensitivity kernels are computed and no inversion is conducted, the two regularization terms at the right hand side of Eq. (37) are not taken into account in this section.

For seismograms recorded at $x = 14.0\,\mathrm{km}$ (Fig. 4a). The direct S wave and the Moho reflected SmS phase for the "true" model arrive closely following the corresponding

SED
6, 2523–2566, 2014

phases in the reference model. As shown in Fig. 5a and b, the geometrical ray paths of both phases are partially within the low velocity zone, and therefore it is reasonable to have delayed S and SmS arrivals in the "true" model. For the sSmS phase, its geometrical ray path does not pass through the low velocity zone but its first Fresnel zone partially coincides with the low velocity anomaly (Fig. 4c). Due to the influence of the low velocity zone, the arrival time of sSmS is delayed by 0.0025 s obtained through cross-correlation calculation. The Fréchet kernels for S, SmS and sSmS are shown in Fig. 5a–c, which closely follows their corresponding geometry ray paths (indicated by dashed lines). The positive Fréchet kernel values in the first Fresnel zones indicate that a reduction of velocity within these regions will result in the reduction of objective function χ. Figures 4b and 5d–f are for the case when seismic waves travel through a high velocity region in the "true" model and seismograms are recorded at the station $x = 86.0$ km. Negative Fréchet kernel values in the first Fresnel zones suggest that an increase of velocity in this region of the reference model can reduce the objective function χ.

The Fréchet kernels displayed in Fig. 5a–f are associated with a particular seismic phase at one seismic station, i.e. the individual kernels. Of course one seismic record does not well constrain the subsurface heterogeneous structure. With the 51 stations on the surface, we could compute the Fréchet kernel for one seismic phase defined at all seismic stations, shown in Fig. 5g–i. These kernels are actually the sum of individual S, SmS and sSmS kernels computed at each station. Due to the increased data coverage and the constructive effect, both the low and high velocity areas are sampled by the bulk part of the kernels. The values of these three kernels are positive within the low velocity zone and negative within the high velocity area, which indicates that updating the velocity model in the opposite direction $-\partial\chi(\boldsymbol{X})/\partial\boldsymbol{X}$ would reduce the objective function χ. We could further define the objective function χ as the sum of S, SmS and sSmS phases at all seismic stations. The corresponding Fréchet kernel is shown in Fig. 6, which is the sum of the kernels in Fig. 5g–i. It can be observed that kernel values at the anomalous regions are not prominent in Fig. 5g–i, but are dominant

SED
6, 2523–2566, 2014

in Fig. 6. This suggests that we may simultaneously use different seismic phase data to highlight anomalous structures in future study. For demonstration purpose, we only worked with one event in this part. To increase the illumination, more seismic events should be included. Once the Fréchet kernels for all events and phases are computed, the LSQR solver or the non-linear conjugate-gradient method can be used to iteratively improve the velocity model.

7 Discussion and conclusions

Wave-equation based traveltime seismic tomography (WETST) involves 2-D forward modelling and 3-D tomographic inversion. Considering adjoint tomography based on 3-D spectral-element method as an approach for "3-D-3-D" seismic tomography (e.g. Tromp et al., 2005; Tape et al., 2009; Zhu et al., 2012), WETST can be viewed as a "2-D-3-D" adjoint tomography technique. From the computation point of view, 2-D forward modelling with a high-order central difference scheme is computationally efficient and can be conducted on most single PCs. This makes it possible to handle large seismic data sets with WETST. Actually, increasing data amount and data coverage is the best way to improve the resolution of tomographic results, and sometimes may compensate for the approximations in the tomography technique itself. For example, it is well known that one main drawback of ray theory is that it does not consider the influence of off-ray structures (Dahlen et al., 2000), but a good data set with a dense and even distribution of ray paths can greatly improve the resolution of ray tomography (Tong et al., 2011). A similar problem for the 2-D approximation in WETST is its ignorance of the off-plane influence on seismic arrivals. To what extent this approximation is valid and how it affects the final inversion results should be further investigated. But taking advantage of the computational efficiency of 2-D forward modelling, we may be able to reduce the effect of the 2-D approximation by increased data coverage in real applications.

WETST only uses traveltime information for two main reasons. First, traveltime is quasi-linear with respect to variations in the velocity structures, which greatly assists

SED
6, 2523–2566, 2014

the convergence of gradient-based inversion methods as presented in Sect. 5. Second, compared with fitting waveforms, it is much easier to predict the arrival times of particular phases on synthetic seismograms computed through 2-D forward modelling. The envelop energy method or the combined ray and cross-correlation method presented in this study can be easily implemented to pick the arrival times on synthetic seismograms.

If 3-D finite-frequency effects need to be taken into account and full waveform fitting is required, we suggest the use of "3-D-3-D" tomographic techniques such as adjoint tomography based on spectral-element method (Tromp et al., 2005; Fichtner et al., 2006). In this case, WETST may be used to construct the starting models for "3-D-3-D" seismic tomography. The hybrid approach could help reduce the total computational costs and speed up the convergence rate of the inverse algorithm as a "closer" initial model is used. Considering that ray-based seismic tomography methods are still the most prevalent tomographic methods and WETST has the advantage of more accurately computed sensitivity kernels, WETST may be a potentially useful compromise for 3-D tomographic inversions before the wider application of "3-D-3-D" seismic tomography in the near future.

Forward modelling in WETST discussed in this paper is based on solving a 2-D acoustic wave equation in the Cartesian coordinates. If the source and the receiver are far away apart and the curvature of the Earth cannot be neglected, the acoustic wave equation in Cartesian coordinates needs to be transformed into geographical coordinates, which may be necessary for the use of teleseismic data. Currently, WETST cannot use converted seismic phases such as *P*–*S* or simultaneously determine the P wave and *S* wave velocity structures in tomographic inversions. But these two goals can be achieved by replacing the 2-D acoustic wave equation with the 2-D elastic wave equation. Additionally, a regular grid with variable grid intervals is suggested to represent the final tomographic results in this paper. To automatically adapt the inversion grid to the data distribution, adaptive mesh using Delaunay triangles and Voronoi polyhedra can be alternatively adopted (e.g. Sambridge and Rawlinson, 2005; Zhang and

SED
6, 2523–2566, 2014

Thurber, 2005; Rawlinson et al., 2010). Source inversion and discontinuity (such as the depth of Moho) determination may also be considered in the future (e.g. Liu and Tromp, 2008; Tong et al., 2014a).

In addition, WETST can include not only direct first arrivals (*P* wave and *S* wave) but also later reflected (e.g. PmP, SmS, pPmP, sSmS) and refracted (Pn, Sn) phases as the ray-based tomographic methods do (e.g. D. Zhao et al., 1992, 2005; Xia et al., 2007). Different seismic phases have different travelling paths and are influenced by structural anomalies differently. The combining use of various seismic phases can increase the illumination of the subsurface structures (Figs. 5 and 6). Since WETST conducts forward modelling in 2-D vertical planes with an efficient high-order central difference scheme, it is possible to include a large set of seismic data in tomographic inversion. Two different inversion algorithms, LSQR solver and the non-linear conjugate-gradient method, can be used to find the optimal tomographic results with efficiency. In a companion paper, we will use WETST to explore the heterogeneous structures beneath the 1992 Landers earthquake (M_w 7.3) area.

Appendix A: High-order central difference method

Yang et al. (2012) developed a finite-difference scheme, nearly-analytic central difference (NACD) method, to solve the 2-D acoustic wave equation. The NACD method has fourth-order accuracies in both space and time, and it uses only three grid nodes in each spatial direction. This method shows a good performance in suppressing numerical dispersions. The essence of the NACD method is to use displacement and its spatial gradient to approximate second and higher order spatial derivatives of the displacement. To achieve this goal, the displacement gradient field is obtained by numerically solving some derived acoustic wave equations (Yang et al., 2012). For simplicity, we use a simplified version of the NACD method to simulate 2-D acoustic wave propagation. In this approach, the value of the spatial gradient along one axis at a particular node is interpolated by the displacement values at its neighbouring grid nodes.

SED
6, 2523–2566, 2014

We call the resultant numerical scheme as the high-order central difference method. The detailed schemes of the high-order central difference method are summarized as follows:

$$\frac{u_{i,j}^{n+1}-2u_{i,j}^{n}+u_{i,j}^{n-1}}{\Delta t^2}-c_{i,j}^2\left(\frac{u_{i+1,j}^{n}-2u_{i,j}^{n}+u_{i-1,j}^{n}}{\Delta x^2}+\frac{u_{i,j+1}^{n}-2u_{i,j}^{n}+u_{i,j-1}^{n}}{\Delta z^2}\right) \tag{A1}$$
$$+\left(\frac{c^2\Delta x^2}{12}-\frac{c^4\Delta t^2}{12}\right)\frac{\partial^4 u}{\partial x^4}\Big|_{i,j}^{n}+\left(\frac{c^2\Delta z^2}{12}-\frac{c^4\Delta t^2}{12}\right)\frac{\partial^4 u}{\partial z^4}\Big|_{i,j}^{n}-\frac{c^4\Delta t^2}{6}\frac{\partial^4 u}{\partial x^2\partial z^2}\Big|_{i,j}^{n}$$
$$=\frac{\partial^2 u}{\partial t^2}\Big|_{i,j}^{n}-c^2\left(\frac{\partial^2 u}{\partial x^2}+\frac{\partial^2 u}{\partial z^2}\right)\Big|_{i,j}^{n}+O(\Delta t^4+\Delta x^4+\Delta z^4)$$

$$\frac{\partial^4 u}{\partial x^4}\Big|_{i,j}^{n}=\frac{1}{\Delta x^4}\left(u_{i+1,j}^{n}-2u_{i,j}^{n}+u_{i-1,j}^{n}\right)+\frac{6}{\Delta x^3}\left(\frac{\partial u}{\partial x}\Big|_{i+1,j}^{n}-\frac{\partial u}{\partial x}\Big|_{i-1,j}^{n}\right)+O(\Delta x^2) \tag{A2}$$

$$\frac{\partial^4 u}{\partial z^4}\Big|_{i,j}^{n}=\frac{1}{\Delta z^4}\left(u_{i,j+1}^{n}-2u_{i,j}^{n}+u_{i,j-1}^{n}\right)+\frac{6}{\Delta z^3}\left(\frac{\partial u}{\partial z}\Big|_{i,j+1}^{n}-\frac{\partial u}{\partial z}\Big|_{i,j-1}^{n}\right)+O(\Delta z^2) \tag{A3}$$

$$\frac{\partial^4 u}{\partial x^2\partial z^2}\Big|_{i,j}^{n}=\frac{1}{\Delta x^2\Delta z^2}\left[2\left(u_{i+1,j}^{n}+u_{i-1,j}^{n}+u_{i,j+1}^{n}+u_{i,j-1}^{n}-2u_{i,j}^{n}\right)-u_{i+1,j+1}^{n}\right. \tag{A4}$$
$$\left.-u_{i-1,j-1}^{n}-u_{i+1,j-1}^{n}-u_{i-1,j+1}^{n}\right]+\frac{1}{2\Delta x\Delta z^2}\left(\frac{\partial u}{\partial x}\Big|_{i+1,j+1}^{n}-\frac{\partial u}{\partial x}\Big|_{i-1,j-1}^{n}\right.$$
$$\left.+\frac{\partial u}{\partial x}\Big|_{i+1,j-1}^{n}-\frac{\partial u}{\partial x}\Big|_{i-1,j+1}^{n}-2\frac{\partial u}{\partial x}\Big|_{i+1,j}^{n}+2\frac{\partial u}{\partial x}\Big|_{i-1,j}^{n}\right)$$
$$+\frac{1}{2\Delta x^2\Delta z}\left(\frac{\partial u}{\partial z}\Big|_{i+1,j+1}^{n}-\frac{\partial u}{\partial z}\Big|_{i-1,j-1}^{n}+\frac{\partial u}{\partial z}\Big|_{i-1,j+1}^{n}-\frac{\partial u}{\partial z}\Big|_{i+1,j-1}^{n}\right.$$
$$\left.-2\frac{\partial u}{\partial z}\Big|_{i,j+1}^{n}+2\frac{\partial u}{\partial z}\Big|_{i,j-1}^{n}\right)+O(\Delta x^2+\Delta z^2)$$

SED
6, 2523–2566, 2014

$$\left.\frac{\partial u}{\partial x}\right|_{i,j}^{n} = \frac{1}{12\Delta x}\left(u_{i-2,j}^{n} - 8u_{i-1,j}^{n} + 8u_{i+1,j}^{n} - u_{i+2,j}^{n}\right) + O(\Delta x^4) \tag{A5}$$

$$\left.\frac{\partial u}{\partial z}\right|_{i,j}^{n} = \frac{1}{12\Delta z}\left(u_{i,j-2}^{n} - 8u_{i,j-1}^{n} + 8u_{i,j+1}^{n} - u_{i,j+2}^{n}\right) + O(\Delta z^4) \tag{A6}$$

The high-order central difference method also has fourth-order temporal accuracy and fourth-order spatial accuracy. Besides, the perfectly matched layer boundary condition is used to absorb the outgoing waves (Komatitsch and Tromp, 2003). To implement this numerical method, the gradients $\partial u/\partial x$ and $\partial u/\partial z$ should be explicitly computed based on formulas (A5) and (A6). Since the gradients of the displacement are computed in forward modelling, the computation of the traveltime sensitivity kernel (Eq. 11) becomes very straightforward, which shows that the high-order central difference method can be naturally adapted for kernel computations.

Acknowledgements. This work was supported by the National Natural Science Foundation of China (Grant No. 41230210), Japan Society for the Promotion of Science (Kiban-S 11050123), and the Discovery Grants of the Natural Sciences and Engineering Research Council of Canada (NSERC, No. 487237 and 490919). X. Y. was partially supported by the Regents Junior Faculty Fellowship of University of California, Santa Barbara. All figures are made with the Generic Mapping Tool (GMT) (Wessel and Smith, 1991).

References

Aki, K. and Lee, W.: Determination of the three-dimensional velocity anomalies under a seismic array using first P arrival times from local earthquakes 1. A homogeneous intial model, J. Geophys. Res., 81, 4381–4399, 1976. 2525, 2528, 2538

Aki, K. and Richards, P. G.: Quantitative Seismology: Theory and Methods, 2nd edn., University Science Books, 2002. 2531

Akram, J.: Automatic P-wave arrival time picking method for seismic and micro-seismic data, CSPG CSEG CWLS Convention, 2011. 2528

SED
6, 2523–2566, 2014

Aster, R. C., Borchers, B., and Thurber, C. H.: Parameter Estimation and Inverse Problems, 2nd edn., Academic Press, 2012. 2544
Baer, M. and Kradolfer, U.: An automatic phase picker for local and teleseismic events, B. Seismol. Soc. Am., 77, 1437–1445, 1987. 2528, 2535
Chen, P., Jordan, T. H., and Zhao, L.: Full 3-D waveform tomography: a comparison between the scattering-integral and adjoint-wavefield methods, Geophys. J. Int., 170, 175–181, 2007a. 2526
Chen, P., Zhao, L., and Jordan, T. H.: Full 3-D tomography for crustal structure of the Los Angeles Region, B. Seismol. Soc. Am., 97, 1094–1120, 2007b. 2526
Coppens, F.: First arrival picking on common-offset trace collections for automatic estimation of static corrections, Geophys. Prospect., 33, 1212–1231, 1985. 2528
Dahlen, F., Nolet, G., and Hung, S.: Fréchet kernels for finite-frequency traveltimes – I. Theory, Geophys. J. Int., 141, 157–174, 2000. 2525, 2528, 2530, 2550
Dahlen, F. A. and Nolet, G.: Comment on "On sensitivity kernels for 'wave-equation' transmission tomography" by de Hoop and van der Hilst, Geophys. J. Int., 163, 949–951, 2005. 2525
de Hoop, M. V. and van der Hilst, R. D.: On sensitivity kernels for "wave-equation" transmission tomography, Geophys. J. Int., 160, 621–633, 2005a. 2525
de Hoop, M. V. and van der Hilst, R. D.: Reply to comment by F. A. Dahlen and G. Nolet on "On sensitivity kernels for 'wave-equation' transmission tomography", Geophys. J. Int., 163, 952–955, 2005b. 2525
Dziewonski, A.: Mapping the lower mantle: determination of lateral heterogeneity in P velocity up to degree and order 6, J. Geophys. Res., 89, 5929–5952, 1984. 2538
Dziewonski, A. M., Hager, B. H., and O'Connell, R. J.: Large-scale heterogeneities in the lower mantle, J. Geophys. Res., 82, 239–255, 1977. 2525
Earle, P. S. and Shearer, P. M.: Characterization of global seismograms using an automatic-picking algorithms, B. Seismol. Soc. Am., 84, 366–376, 1994. 2528, 2535
Fichtner, A. and Trampert, J.: Resolution analysis in full waveform inversion, Geophys. J. Int., 187, 1604–1624, 2011. 2526
Fichtner, A., Bunge, H. P., and Igel, H.: The adjoint method in seismology I. Theory, Phys. Earth Planet. In., 157, 86–104, 2006. 2526, 2528, 2551
Fichtner, A., Igel, H., Bunge, H.-P., and Kennett, B. L. N.: Simulation and inversion of seismic wave propagation on continental scales based on a spectral-element method, J. Numer. Anal. Indust. Appl. Math., 4, 11–22, 2009. 2526

SED
6, 2523–2566, 2014

Fletcher, R. and Reeves, C.: Function minimization by conjugate gradients, Comput. J., 7, 149–154, 1964. 2546
Gautier, S., Nolet, G., and Virieux, J.: Finite-frequency tomography in a crustal environment: application to the western part of the Gulf of Corinth, Geophys. Prospect., 56, 493–503, 2008. 2525
Graves, R. W.: Simulating seismic wave propagation in 3-D elastic media using staggered-grid finite differences, B. Seismol. Soc. Am., 86, 1091–1106, 1996. 2539
Han, L., Wong, J., and Bancroft, J.: Time picking on noisy microseismograms, GeoCanada, 2010. 2528, 2534
Hung, S., Shen, Y., and Chiao, L.: Imaging seismic velocity structure beneath the Iceland hot spot: a finite frequency approach, J. Geophys. Res., 109, B08305, doi:10.1029/2003JB002889, 2004. 2525
Hung, S. H., Chen, W. P., and Chiao, L. Y.: A data-adaptive, multiscale approach of finite-frequency, traveltime tomography with special reference to P and S wave data from central Tibet, J. Geophys. Res., 116, B06307, doi:10.1029/2010JB008190, 2011. 2525, 2527
Kennett, B. L. N. and Engdah, E. R.: Traveltimes for global earthquake location and phase identification, Geophys. J. Int., 105, 429–465, 1991. 2528
Kim, Y., Liu, Q., and Tromp, J.: Adjoint centroid-moment tensor inversions, Geophys. J. Int., 186, 264–278, 2011. 2546
Komatitsch, D. and Tromp, J.: Introduction to the spectral element method for three-dimensional seismic wave propagation, Geophys. J. Int., 139, 806–822, 1999. 2539
Komatitsch, D. and Tromp, J.: Spectral-element simulations of global seismic wave propagation – I. Validation, Geophys. J. Int., 149, 390–412, 2002a. 2525
Komatitsch, D. and Tromp, J.: Spectral-element simulations of global seismic wave propagation – II. 3-D models, oceans, rotation, and self-gravitation, Geophys. J. Int., 150, 303–318, 2002b. 2525
Komatitsch, D. and Tromp, J.: A perfectly matched layer absorbing boundary condition for the second-order seismic wave equation, Geophys. J. Int., 154, 146–153, 2003. 2554
Komatitsch, D., Liu, Q., Tromp, J., Suss, M. P., Stidham, C., and Shaw, J. H.: Simulations of ground motion in the Los Angeles Basin based upon the spectral-element method, B. Seismol. Soc. Am., 94, 187–206, 2004. 2525

SED
6, 2523–2566, 2014

Komatitsch, D., Erlebacher, G., Göddeke, D., and Michéa, D.: High-order finite-element seismic wave propagation modeling with MPI on a large GPU cluster, J. Comput. Phys., 229, 7692–7714, 2010. 2527
Lee, H. Y., Koo, J. M., Min, D. J., Kwon, B. D., and Yoo, H. S.: Frequency-domain elastic full waveform inversion for VTI media, Geophys. J. Int., 183, 884–904, 2010. 2526
Li, C., van der Hilst, R. D., and Toksoz, N. M.: Constraining spatial variations in P-wave velocity in the upper mantle beneath Southeast Asia, Phys. Earth Planet. In., 154, 180–195, 2006. 2544
Li, C., van der Hilst, R. D., Engdahl, E. R., and Burdick, S.: A new global model for P wave speed variations in Earth's mantle, Geochem. Geophys. Geosyst., 9, Q05018, doi:10.1029/2007GC001806, 2008. 2527, 2544
Liu, Q. and Gu, Y. J.: Seismic imaging: from classical to adjoint tomography, Tectonophysics, 566–567, 31–66, 2012. 2525, 2526
Liu, Q. and Tromp, J.: Finite-frequency kernels based on adjoint methods, B. Seismol. Soc. Am., 96, 2283–2297, 2006. 2526
Liu, Q. and Tromp, J.: Finite-frequency sensitivity kernels for global seismic wave propagation based upon adjoint methods, Geophys. J. Int., 174, 265–286, 2008. 2526, 2552
Liu, Q., Polet, J., Komatitsch, D., and Tromp, J.: Spectral-element moment tensor inversions for earthquakes in southern California, B. Seismol. Soc. Am., 94, 1748–1761, 2004. 2537
Luo, Y. and Schuster, G.: Wave equation inversion of skeletonized geophysical data, Geophys. J. Int., 105, 289–294, 1991. 2528
Maggi, A., Tape, C. H., Chen, M., Chao, D., and Tromp, J.: An automated time-window selection algorithm for seismic tomography, Geophys. J. Int., 178, 257–281, 2009. 2528, 2535
Marquering, H., Dahlen, F., and Nolet, G.: Three-dimensional sensitivity kernels for finite-frequency traveltimes: the banana-doughnut paradox, Geophys. J. Int., 137, 805–815, 1999. 2525
Michéa, D. and Komatitsch, D.: Accelerating a three-dimensional finite-difference wave propagation code using GPU graphics cards, Geophys. J. Int., 182, 389–402, 2010. 2527
Montelli, R., Nolet, G., Dahlen, A., Masters, G., Robert Engdahl, E., and Hung, S.: Finite-frequency tomography reveals a variety of plumes in the mantle, Science, 303, 338–343, 2004. 2525
Munro, K. A.: Automatic event detection and picking P-wave arrivals, CREWES Research Report, 18, 12.1-12.10, 2004. 2535

SED
6, 2523–2566, 2014

Nolet, G., Dahlen, F. A., and Montelli, R.: Traveltimes and amplitudes of seismic waves: a re-assessment, in: Seismic Earth: Array Analysis of Broadband Seismograms, edited by: Levander, A. and Nolet, G., 37–47, AGU, 2005. 2538, 2540

Operto, S., Virieux, J., Dessa, J. X., and Pascal, G.: Crustal seismic imaging from multifold ocean bottom seismometer data by frequency domain full waveform tomography: application to the eastern Nankai trough, J. Geophys. Res., 111, B09306, doi:10.1029/2005JB003835, 2006. 2526

Operto, S., Virieux, J., Amestoy, P., L'Excellent, J. Y., Giraud, L., and Ben Hadj Al, H.: 3-D finite-difference frequency-domain modeling of visco-acoustic wave propagation using a massively parallel direct solver: a feasibility study, Geophysics, 72, SM195–SM211, doi:10.1190/1.2759835 2007. 2525

Paige, C. and Saunders, M.: LSQR: An algorithm for sparse linear-equations and sparse least-squares, Trans. Maths Software, 8, 43–71, 1982. 2545

Pratt, R. G. and Shipp, R. M.: Seismic waveform inversion in the frequency domain, part 2: fault delineation in sediments using crosshole data, Geophysics, 64, 902–914, 1999. 2526

Rawlinson, N., Pozgay, S., and Fishwick, S.: Seismic tomography: a window into deep earth, Phys. Earth Planet. In., 178, 101–135, 2010. 2525, 2539, 2544, 2545, 2552

Rickers, F., Fichtner, A., and Trampert, J.: The Iceland-Jan Mayen plume system and its impact on mantle dynamics in the North Atlantic region: evidence from full-waveform inversion, Earth Planet. Sc. Lett., 367, 39–51, 2013. 2526

Romanowicz, B.: Seismic tomography of the Earth's mantle, Annu. Rev. Earth Pl. Sci., 19, 77–99, 1991. 2525

Saari, J.: Automated phase picker and source location algorithm for local distances using a single three-component seismic station, Tectonophysics, 189, 307–315, 1991. 2528, 2534

Sambridge, M. and Rawlinson, N.: Seismic tomography with irregular meshes, in: Seismic earth: array analysis of broadband seismograms, edited by Lavender, A. and Nolet, G., Geophysical Monograph, 49–65, AGU, Washington, D. C., 2005. 2551

Tape, C., Liu, Q., and Tromp, J.: Finite-frequency tomography using adjoint methods-methodology and examples using membrane surface waves, Geophys. J. Int., 168, 1105–1129, 2007. 2525, 2526, 2528, 2539, 2546

Tape, C., Liu, Q., Maggi, A., and Tromp, J.: Adjoint tomography of the southern California crust, Science, 325, 988–992, 2009. 2526, 2527, 2546, 2550

SED
6, 2523–2566, 2014

Tape, C., Liu, Q., Maggi, A., and Tromp, J.: Seismic tomography of the southern California crust based on spectral-element and adjoint methods, Geophys. J. Int., 180, 433–462, 2010. 2526
Tarantola, A.: Inversion of seismic reflection data in the acoustic approximation, Geophysics, 49, 1259–1266, 1984. 2526
Tarantola, A.: Inverse Problem Theory and Methods for Model Parameter Estimation, 1st edn., Society for Industrial and Applied Mathematics, Philadelphia, 2005. 2544
Thurber, C. H.: Earthquake locations and three-dimensional crustal structure in the Coyote Lake area, central California, J. Geophys. Res., 88, 8226–8236, 1983. 2538
Tian, Y., Montelli, R., Nolet, G., and Dahlen, F.: Computing travel-time and amplitude sensitivity kernels in finite-frequency tomography, J. Comput. Phys., 226, 2271–2288, 2007. 2525
To, A. and Romanowicz, B.: Finite frequency effects on global S diffracted traveltimes, Geophys. J. Int., 179, 1645–1657, 2009. 2525
Tong, P., Zhao, D., and Yang, D.: Tomography of the 1995 Kobe earthquake area: comparison of finite-frequency and ray approaches, Geophys. J. Int., 187, 278–302, 2011. 2525, 2531, 2550
Tong, P., Zhao, D., and Yang, D.: Tomography of the 2011 Iwaki earthquake (M 7.0) and Fukushima nuclear power plant area, Solid Earth, 3, 43–51, doi:10.5194/se-3-43-2012, 2012. 2527, 2534
Tong, P., Chen, C.-W., Komatitsch, D., Basini, P., and Liu, Q.: High-resolution seismic array imaging based on an SEM-FK hybrid method, Geophys. J. Int., 197, 369–395, 2014a. 2526, 2539, 2552
Tong, P., Zhao, D., Yang, D., Yang, X., Chen, J., and Liu, Q.: Wave-equation based traveltime seismic tomography – Part 2: Application to the 1992 Landers earthquake (M_w 7.3) area, Solid Earth Discuss., 5, 2567–2613, doi:10.5194/sed-5-2567-2014, 2014b. 2529
Tromp, J., Tape, C., and Liu, Q.: Seismic tomography, adjoint methods, time reversal and banana-doughnut kernels, Geophys. J. Int., 160, 195–216, 2005. 2526, 2528, 2530, 2531, 2546, 2550, 2551
Virieux, J.: SH-wave propagation in heterogeneous media: velocity-stress finite difference method, Geophysics, 49, 1933–1942, 1984. 2539
Virieux, J. and Operto, S.: An overview of full-waveform inversion in exploration geophysics, Geophysics, 74, WCC1–WCC26, 2009. 2526
Wessel, P. and Smith, W. H. F.: Free software helps map and display data, EOS T. Am. Geophys. Un., 72, 441–448, 1991. 2554

SED
6, 2523–2566, 2014

Wong, J., Han, L., Bancroft, J., and Stewart, R.: Automatic time-picking of first arrivals on noisy microseismic data, CSEG, 2009. 2535
Xia, S., Zhao, D., Qiu, X., Nakajima, J., Matsuzawa, T., and Hasegawa, A.: Mapping the crustal structure under active volcanoes in central Tohoku, Japan using P and PmP data, Geophys. Res. Lett., 34, L10309, doi:10.1029/2007GL030026, 2007.
Yang, D., Tong, P., and Deng, X.: A central difference method with low numerical dispersion for solving the scalar wave equation, Geophys. Prospect., 60, 885–905, 2012. 2552
Zhang, H. and Thurber, C.: Adaptive-mesh seismic tomography based on tetrahedral and Voronoi diagrams: application to Parkfield, California, J. Geophys. Res., 110, B04303, doi:10.1029/2004JB003186, 2005. 2551
Zhang, H., Thurber, C., and Rowe, C.: Automatic P Wave arrival detection and picking with multiscale wavelet analysis for single-component recordings, B. Seismol. Soc. Am., 93, 1904–1912, 2003. 2528
Zhao, D.: Multiscale seismic tomography and mantle dynamics, Gondwana Res., 15, 297–323, 2009. 2539
Zhao, D.: Tomography and dynamics of Western-Pacific subduction zones, Monogr. Environ. Earth Planets, 1, 1–70, 2012. 2525
Zhao, D., Hasegawa, A., and Horiuchi, S.: Tomographic imaging of P and S wave velocity structure beneath northeastern Japan, J. Geophys. Res., 97, 19909–19928, 1992. 2528, 2542
Zhao, D., Todo, S., and Lei, J.: Local earthquake reflection tomography of the Landers aftershock area, Earth. Planet. Sc. Lett., 235, 623–631, 2005. 2548
Zhao, D., Yanada, T., Hasegawa, A., Umino, N., and Wei, W.: Imaging the subducting slabs and mantle upwelling under the Japan Islands, Geophys. J. Int., 190, 816–828, 2012. 2527
Zhao, L. and Jordan, T. H.: Structural sensitivities of finite-frequency seismic waves: a full-wave approach, Geophys. J. Int., 165, 981–990, 2006. 2525
Zhao, L., Jordan, T. H., and Chapman, C. H.: Three-dimensional Fréchet differential kernels for seismic delay times, Geophys. J. Int., 141, 558–576, 2000. 2525
Zhao, L., Jordan, T. H., Olsen, K. B., and Chen, P.: Fréchet kernels for imaging regional earth structure based on three-dimensional reference models, B. Seismol. Soc. Am., 95, 2066–2080, 2005. 2526
Zhu, H., Bozdag, E., Peter, D., and Tromp, J.: Structure of the European upper mantle revealed by adjoint tomography, Nat. Geosci., 5, 493–498, 2012. 2526, 2527, 2546, 2550

SED
6, 2523–2566, 2014

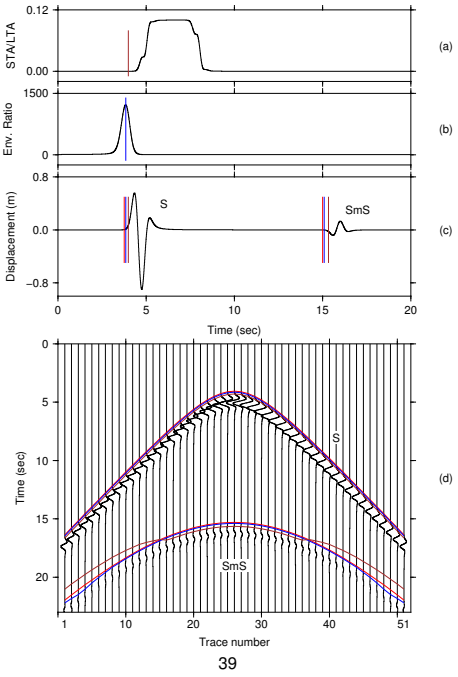

39

Figure 1. *S* arrival time-picking using **(a)** the STA/LTA method and **(b)** the envelop energy ratio (EER) method for the synthetic seismogram in **(c)**, which is the seismogram for trace number 26 in **(d)**. **(d)** Displays synthetic seismograms recorded by 51 stations with an equal spacing of 2 km at the surface, which are generated by an earthquake at the depth 12.0 km directly below the 26th station. The computational domain is a crust over mantle model. The crust has a thickness of 30.0 km and is homogeneous with the *S* wave velocity 3.2 km s^{-1} in the crust and 4.5 km s^{-1} in the mantle. In **(c)** and **(d)**, the arrival times of S and SmS phases determined based on the STA/LTA and EER methods are labelled with brown and blue lines, respectively. The theoretical arrivals are marked by red lines.

SED
6, 2523–2566, 2014

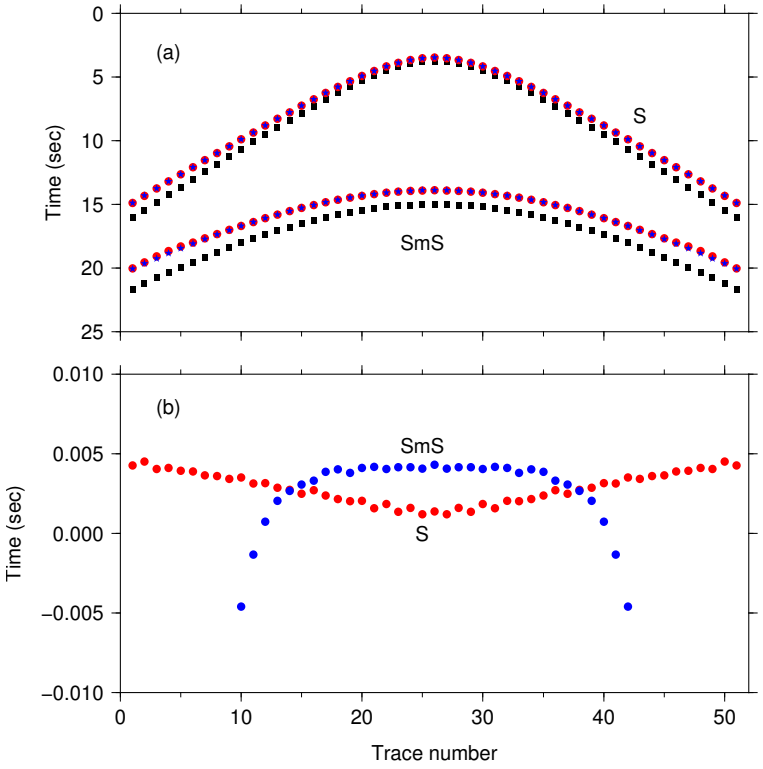

Figure 2. (a) S and SmS arrival times on seismograms computed in two models $\boldsymbol{m}_0$ and $\boldsymbol{m}_1$. Numerical computation in $\boldsymbol{m}_0$ is the same as the example shown in Fig. 1. *S* wave velocity in $\boldsymbol{m}_1$ has a perturbation of 8 % with respect to $\boldsymbol{m}_0$. Black squares, red circles, and blue stars are corresponding to theoretical arrival times in $\boldsymbol{m}_0$, theoretical arrival times in $\boldsymbol{m}_1$, and arrival times computed by using the combined ray and cross-correlation method, respectively. **(b)** Errors of S (red circles) and SmS (blue circles) arrival times determined by using the combined ray and cross-correlation method.

SED
6, 2523–2566, 2014

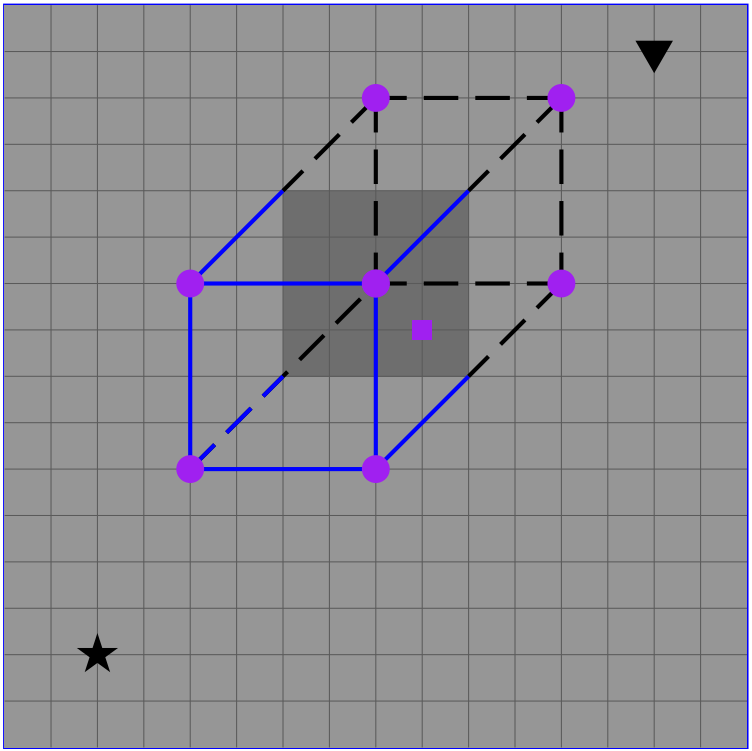

Figure 3. Linear interpolation of the material properties on one forward modelling grid node (purple square) with material properties on its eight surrounding inversion grid nodes (purple circles). Forward modelling grid is a regular 2-D mesh with fixed grid intervals (formed by grey lines), and inversion grid is a 3-D regular mesh with variable grid intervals. Black star and black inverse triangle denote the locations of the earthquake and seismic station in the 2-D vertical plane, respectively.

SED
6, 2523–2566, 2014

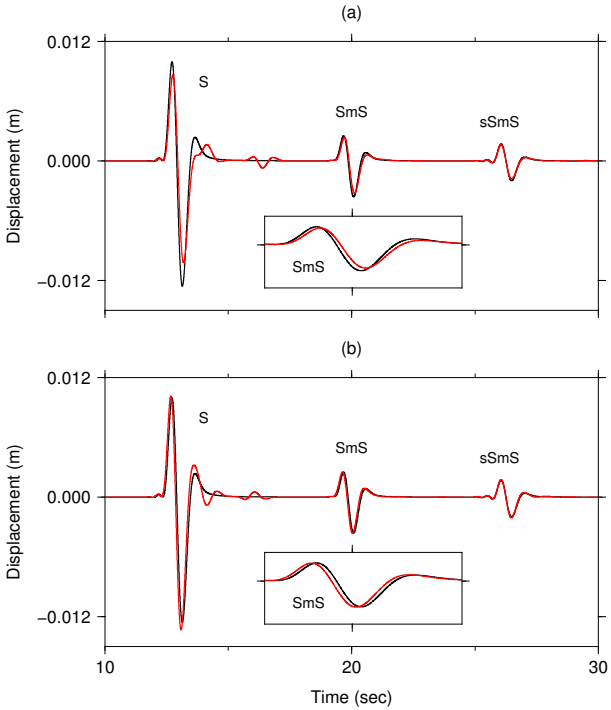

Figure 4. Seismograms recorded by the stations located at **(a)** x = 14 km and **(b)** x = 86 km on the surface. Seismograms computed in the reference model are shown as black curves, and those computed in the "true" model are illustrated by red curves. The computational domain is a crust over mantle model with a size of 100 km × 50 km. The crust has a thickness of 30 km containing one low and one high velocity zone in the "true" model respect to the reference model (Fig. 5). The earthquake is located at x = 50 km at the depth 12 km.

SED
6, 2523–2566, 2014

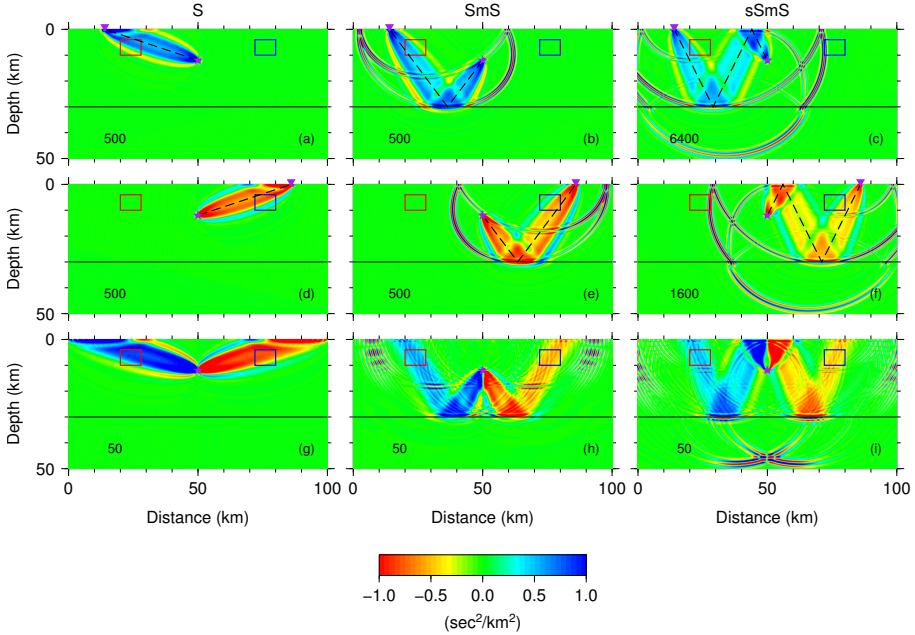

Figure 5. Fréchet kernels corresponding to direct S **(a, d, g)**, SmS **(b, e, h)** and sSmS **(c, f, i)** phases. **(a)–(c)** Are computed only using seismograms recorded at the station $x = 14$ km. These seismograms are influenced by the low velocity zone in the red box in the "true" model. **(d)–(f)** Are only related to seismograms recorded at the station $x = 86$ km, which are influenced by the high velocity zone in the blue box in the "true" model. **(g)–(i)** Are computed for all 51 stations on the surface. To use a uniform colour bar indicated at the bottom for all subfigures, each kernel is amplified by multiplying the number at the left bottom of the corresponding subfigure.

SED
6, 2523–2566, 2014

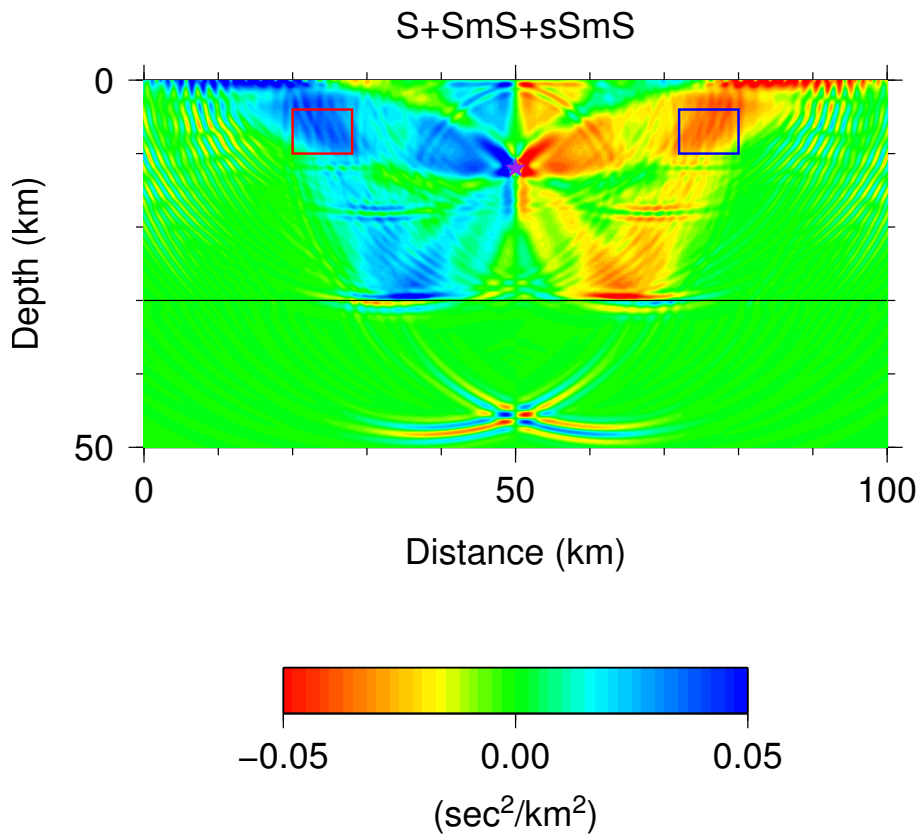

Figure 6. Summation of the Fréchet kernels corresponding to the kernels for S, SmS and sSmS phases in Fig. 5g–i.

SED
6, 2523–2566, 2014